TÉCNICO LISBOA

A robot-assisted 3D US image-guided tool for liver tumor tracking

Nuno Daniel da Silva Rodrigues

Thesis to obtain the Master of Science Degree in

Biomedical Technologies

Supervisor: Prof. Jorge Manuel Mateus Martins

Examination Committee

Chairperson: Prof. Patrícia Margarida Piedade Figueiredo

Supervisor: Prof.Jorge Manuel Mateus Martins

Member of the Committee: Prof. João Miguel Raposo Sanches

October, 2017

Acknowledgments

I would like to use this page to express some thoughts and well due acknowledgements to everyone that in some way contributed for this project.

On a first instance, I would like to express my gratitude to Prof. Jorge Martins for the opportunity to join the Surgical Robots Laboratory group, for all the tutoring and valuable debates. I would also like to thank to all the colleagues in the lab for their availability and companionship, particularly to Pawel, Rui and Ricardo for the useful advices and crucial assistance!

Secondly, it is crucial to recognize that some of the developed components of this project profited greatly from the contribution and patronage of some well established companies. More precisely CIRS, Inc (in the person of Ted Lynch), The Linde Group (Linde AG) and Rogério Rocha, from ABGT, Lda. To all of them my honest salutation, without their contribution it would have been much harder.

Finally, I am thankful to my family and friends for their support, to António Antunes for his camaraderie during all the long nights working and especially to Joana Oliveira for her love, support and meticulous proofreading.

This was definitely a very important journey of my life, a proof of determination and will. Completing it required a great deal of effort, endurance and sacrifice. At the end, it was worth it!

Resumo

Atualmente, as técnicas de radioterapia são altamente dependentes da imagem quer para a correcção do posicionamento do doente, como para a monitorização de movimento. O método padrão para monitorização de tumores durante radioterapia no fígado recorre à fluoroscopia para identificação de Marcadores Fiduciais (FM). A imagem de US 3D fornece informação volumétrica, elevado contraste de tecido mole e é não ionizante. Fixando a sonda com um braço robótico, cria uma ferramenta com potencial para a monitorização de tumores em tempo real permitindo a aquisição contínua de imagem remotamente.

Este estudo propõe o desenvolvimento de uma ferramenta de imagem guiada assistida por robótica para o posicionamento de doentes e monitorização de tumores do fígado durante radioterapia. Foca-se, especialmente, na utilização de métodos de registo deformável sob a hipótese de que utilizando este tipo de algoritmos o impacto da deformação do tecido pode ser minimizado, resultando numa avaliação mais precisa do desvio tumoral. Foram implementados algoritmos de registo de imagem baseados em transformações *Affine* e *Demons*.

Os resultados mostram que, definindo uma região de interesse, todos os métodos atingem um erro médio inferior a 1 mm. Contrariamente, utilizando a imagem completa os algoritmos *demons* e híbrido apresentam um desempenho bastante superior.

O algoritmo de registo *demons* demonstra ser o mais adequado para a aplicação proposta. Quando combinado com uma ferramenta de imagem guiada assistida por robótica para a aquisição contínua de imagens de US 3D, apresenta potencial para substituir a utilização de FM em técnicas de radioterapia guiada por imagem no fígado.

Keywords: IGRT, 3D US, KUKA Lightweight Robot, Deformable Image Registration.

Abstract

Advanced radiotherapy is highly dependent on imaging modalities for both patient set-up correction and motion management during treatment. The current gold-standard method for tumor motion tracking in the liver resorts to the use of X-Ray fluoroscopy for FM identification during treatment delivery. 3D US imaging provides volumetric information, high soft tissue contrast and is non-ionizing. When fixated by a robotic arm, it creates a valid and useful tool for real-time tumor motion monitoring, while enabling remote continuous image acquisition.

This study proposes the development of a robotic assisted 3D US image-guided tool for correct patient set-up and accurate tumor motion monitoring during radiotherapy in the liver. It focuses, especially, in the use of deformable image registration approaches, hypothesizing that these types of algorithms could minimize the impact of tissue deformation resulting in a more accurate displacement measurement. Affine, demons and hybrid image registration algorithms were implemented for this purpose.

Obtained results show that, when a ROI is defined, all methods work exceptionally well, with mean errors bellow 1 mm. Oppositely, when the whole image information is used, demons and hybrid registration methods appear to perform better and more consistently, being less influenced by the information contained in the FOV.

Demons image registration demonstrates to be the most adequate method for the proposed application. When combined with a robotic-US setup for adequate continuous 3D US image acquisition it becomes a powerful tool that presents the possibility to overcome the use of FM as surrogates for IGRT techniques in the liver.

Keywords: IGRT, 3D US, KUKA Lightweight Robot, Deformable Image Registration.

Contents

List of Tables

List of Figures

1. Introduction

1.1. *Objectives/Aims*

The presented work aims at the use of 3D ultrasound (US) imaging, registered onto a reference US image, assisted by a robotic arm, for accurate tracking of identified targets within soft tissue such as the liver. Ideally, the same ultrasound-robot setup is to be used for tracking the organ in real-time in order to monitor target motion during external beam radiation therapy.

1.2. *Rationale*

Modern radiotherapy treatments are highly dependent on imaging modalities for both patient set-up correction and motion management during treatment – Image-guided Radiation Therapy (IGRT).

The current gold-standard method for tumor motion tracking in the liver resorts to the implantation of fiducial markers (FM) as surrogates to the tumor and their posterior identification and tracking during treatment delivery. However, this approach has some limitations: their accuracy is directly dependent on the tumor-marker distance [1]; the only real-time available method for FM tracking is x-ray fluoroscopy, which uses ionizing radiation and does not provide information on soft-tissue; and the implantation method by itself is inaccurate if performed manually [2], [3].

US imaging provides high soft tissue contrast and is non-ionizing. When coupled with a fixation device such as a robotic arm, it provides a valid and useful tool for real-time motion monitoring in radiotherapy by allowing continuous image acquisition without the physical presence of the staff inside the treatment room. The robotic arm motion and force control characteristics allow for the reduction of tissue deformation due to probe pressure, increasing the reproducibility and application scenarios of such systems. At the same time the position control feature of the robotic arm in use guarantees that the probe remains still during image acquisition of moving targets. This is of extreme importance for the experiments that will be carried out and for the application itself as it ensures proper image acquisition with almost no deviation errors induced by probe miss-positioning or variation.

Robotic image-guided tools have been proven to be useful in percutaneous interventions like biopsies or the implantation of FM [4–6]. Nevertheless, these tools also allow for direct tissue identification and tracking, potentially overcoming the need for the implantation of FM [7, 8].

This study proposes the development of a robotic assisted image-guided tool capable of providing information for correct patient set-up and performing accurate tumor motion monitoring, during radiotherapy treatment delivery in the liver. The core developments and experiments of this work will address the hypothesis that applying non-rigid image registration algorithms may be an accurate approach for displacement measurements in liver lesions, given that the additional Degrees of Freedom (DoF) allow for the compensation of tissue deformation and compression outperforming rigid approaches and even manual image registration in the assessment of tumor motion.

1.3. *Thesis Outline*

The unraveling of this document is structured in a total of 5 chapters.

The first and present one focuses on the aims of the study, presenting the rationale and underlying motivation and frames the document that follows by introducing its outline.

The second chapter pursuits the introduction of several subjects that are considered crucial to understand the relevance of the proposed application. The liver anatomy is briefly explained and a short depiction of the most common liver tumors is done, also describing their characteristic echogenic behavior. The existing IGRT techniques are highlighted and focus is given to other studies and applications that follow a similar approach as this study. An introduction is made to image registration and finally the relevant existing image registration algorithms are explained.

On the third chapter, the implementation stages are exposed, describing several of the tools that were required to be developed during the experiment such as the 4D liver phantom, the Robot-US probe coupling tool and the 3D image registration application. The robot setup is detailed and the integrated system and its components are explained.

The fourth chapter presents the tests that were performed and the achieved outcomes, followed by their respective discussion.

This document is terminated with the fifth chapter in which the author presents his conclusion on the final products of this work. Some suggestions are given relating future experiments, developments and possible improvements.

2. Theoretical Overview

2.1. ***Liver tumors***

The liver is the largest gland of the human body and the second largest organ (after the skin), weighing approximately 1500 g. It lies under the diaphragm in the right abdomen and midabdomen and extends to the left upper abdomen. It has an overall wedge shape, which is in part determined by the form of the upper abdominal cavity into which it grows. It is usually reddish brown in color and varies from soft to firm in texture (*Figure 1*) [9].

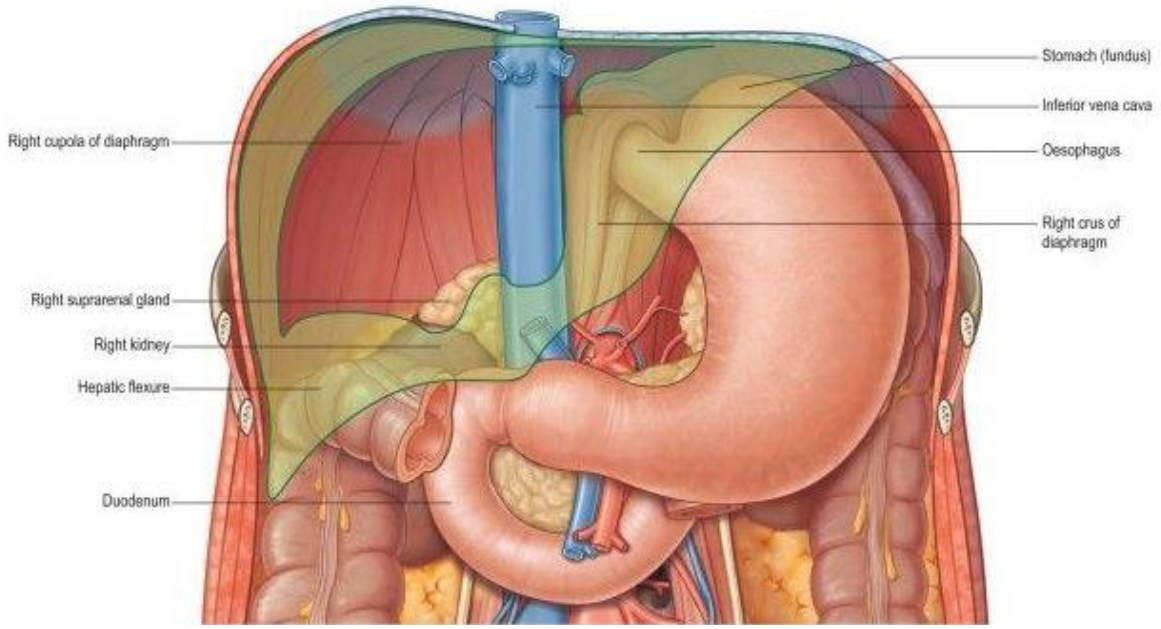

Figure 1 - Liver 'bed'. The outline of the liver is shaded in green. The central bare area is unshaded. [9]

The liver performs a wide range of metabolic activities required for homeostasis, nutrition and immune defense, such as removal and break down of toxic materials from the blood, regulation of blood glucose and lipids and production of thermal energy. It receives its blood supply from two sources: 80% is delivered by the portal vein, which drains the spleen and intestines; and the remaining 20%, the oxygenated blood, is delivered by the hepatic artery [9, 10].

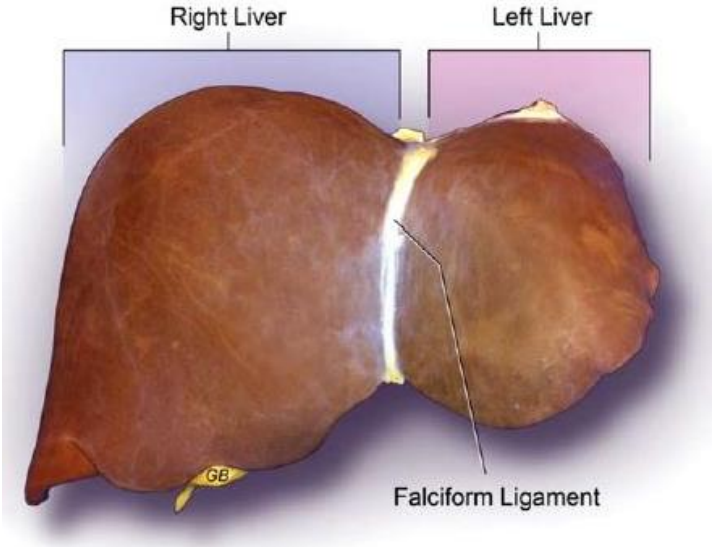

Figure 2 - External liver anatomy - Right and left lobes divided by the falciform ligament. [10]

Externally it is divided by the falciform ligament into a larger right lobe and a smaller left lobe (*Figure 2*) and functionally the liver is divided into eight independent segments, each one having its portal pedicle consisting of the hepatic arterial branch, portal branch, and the bile duct with a separate hepatic venous branch that provides outflow (*Figure 3*) [10].

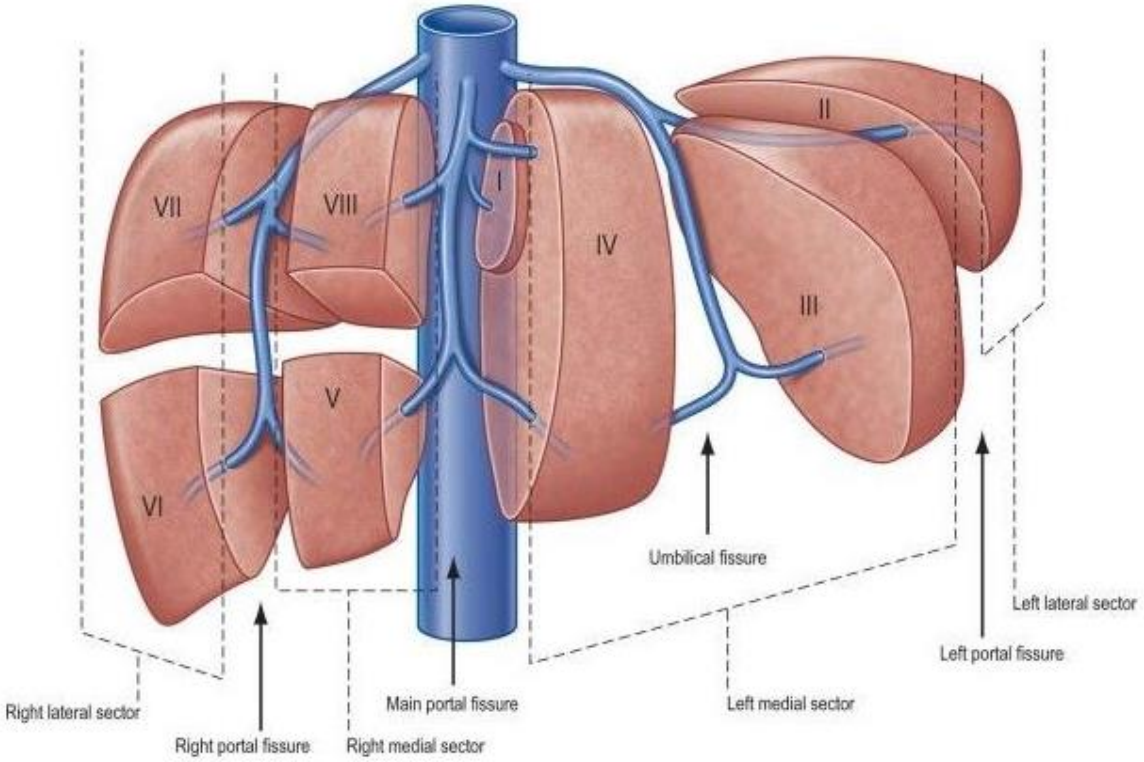

Figure 3 - Sectors and segments of the liver. Right lateral = right posterior; Right medial = right anterior.[9]

The liver is an important organ from an oncologic perspective since this is the most common site of metastasis from gastrointestinal tumors. Besides metastatic disease, the incidence of primary liver malignancies has been increasing over the last 20 years, particularly Hepatocellular Carcinoma (HCC), globally the commonest liver primary, and Cholangiocarcinoma (CCA), registered as the second most common primary liver tumor. HCC is presently one of the most common causes of cancer death worldwide and the fifth most common cancer overall. CCA shares 3% of all gastrointestinal cancers and has been increasing rapidly [11, 12].

B-mode US is often the first line investigation in liver disease, being outlined in the British Society of Gastroenterologists (BSG) guidelines for diagnosis of both HCC and CCA in adults [12]. According to the existing literature, the multiplanar capabilities of US are well suited to the identification of the anatomical landmarks and therefore to the precise localization of focal liver lesions [13]. These statements validate the use of US imaging target tracking in the liver and the sonographic appearance of the previously mentioned types of malignancies will be described in the following paragraphs.

2.1.1. **Hepatocellular Carcinoma (HCC)**

Pathologically, HCC occurs in three forms: solitary, multiple nodules and diffuse infiltrative. The sonographic appearance is variable, but there is a relation to size.

Small HCC tumors (< 3 cm) usually show a nodular configuration and can be divided into four types: single nodular type, single nodular type with extranodular growth, contiguous multinodular type, and poorly demarcated nodular type. Small HCCs tend to be hypoechoic (*Figure 4*). Increasing echogenicity is related to the presence of hemorrhage, fibrosis and necrosis, echogenic lesions being found in about one half of large HCCs. Small HCCs may also appear hyperechoic due to fatty change or sinusoidal dilatation.

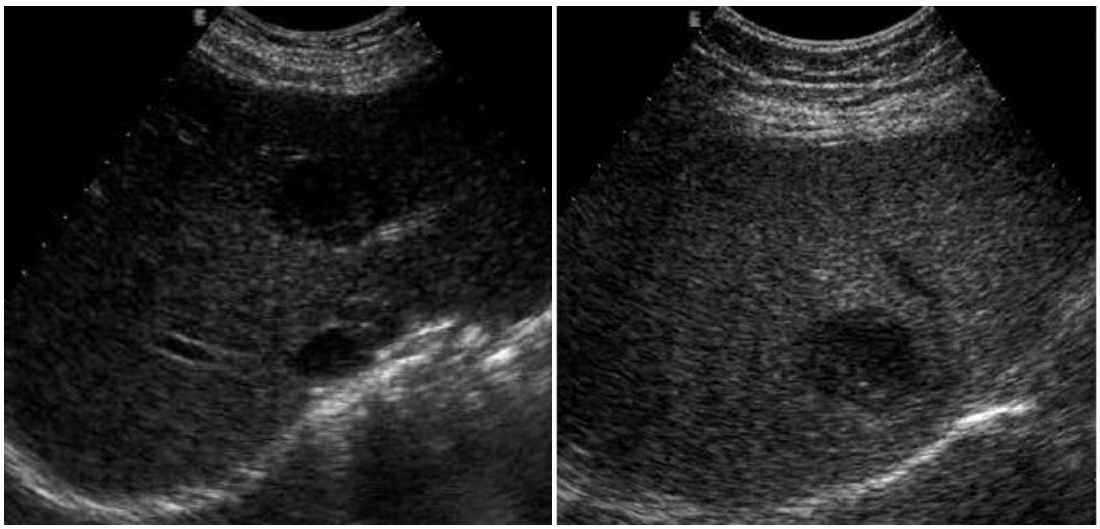

Figure 4 - Example of two small sized HCC with hypoechoic sonographic appearance.[13]

Advanced HCC tumors are classified into three major types: nodular, expansive type; massive, infiltrative type; and diffuse type. The typical nodular, expansive type HCC is a sharply demarcated lesion that may be unifocal or multifocal. Large, nodular type HCC typically shows inhomogeneous internal architecture with components of different echogenicity separated by thin *septa* (mosaic pattern). Most expansive type HCCs have a well-developed fibrous capsule that shows itself as a peripheral hypoechoic halo (*Figure 5*). The infiltrative type HCC is characterized by an irregular and indistinct tumor-nontumor boundary [13, 14].

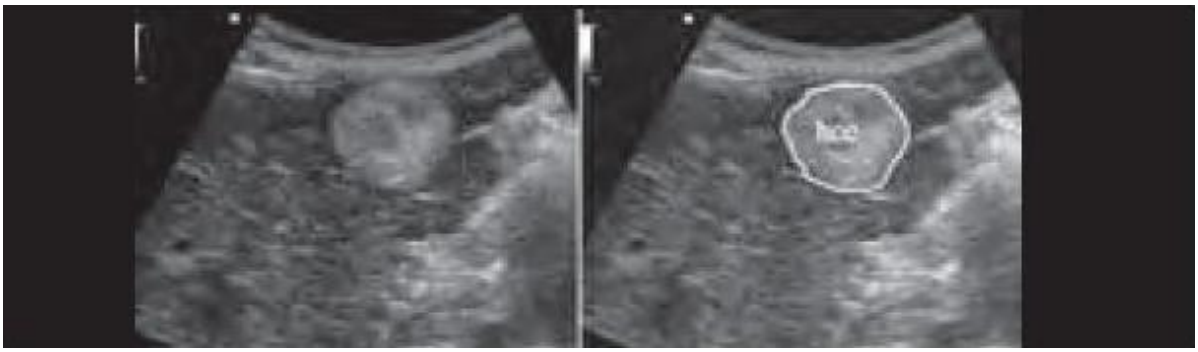

Figure 5 - Hyperechoic, inhomogeneous HCC with hypoechoic halo.[14]

2.1.2. **Cholangiocarcinoma (CCA)**

Mass-forming intra-hepatic CCA manifests as a solitary mass in liver parenchyma with a nodular pattern. Increasing tumor echogenicity together with increasing tumor size is a well-documented finding.

On sonography, most occur as a single, homogeneous, hypoechoic mass. When detected, they are usually ill defined and poorly reflective (*Figure 6*). Nodules less than 3 cm tend to be hypoechoic or isoechoic, whereas lesions greater than 3 cm are predominantly hyperechoic.

When multiple lesions are present, the larger mass shows higher echogenicity compared to the daughter nodules. A peripheral hypoechoic area, so-called halo sign, is observed in 1/3 of all cases. These US findings do not differ from those found in cases of metastases from extrahepatic adenocarcinomas, which have also histological similarities. Sometimes, the central portion of the tumor may appear hypoechoic, due to the presence of necrosis, or markedly hyperechoic with acoustic shadowing, due to the presence of calcifications [12-14].

Figure 6 - Large hepatic CCA - ill-defined, heterogeneous and hypoechoic mass (arrows) with multiple intra-tumoral echogenic spots.[14]

2.1.3. **Metastasis**

Although there are no absolutely confirmatory features of metastatic disease on sonography, the presence of multiple solid nodules of different sizes and the presence of a hypoechoic halo surrounding a liver mass are indicative of metastasis. The echo patterns of metastases are numerous (*Figure 7)*, but some patterns are said to be commonly associated with certain primary tumors. Most metastasis are round with well-defined margins. Hypoechoic metastasis are more common (approximately 65%) than hyper- or isoechoic [13, 14].

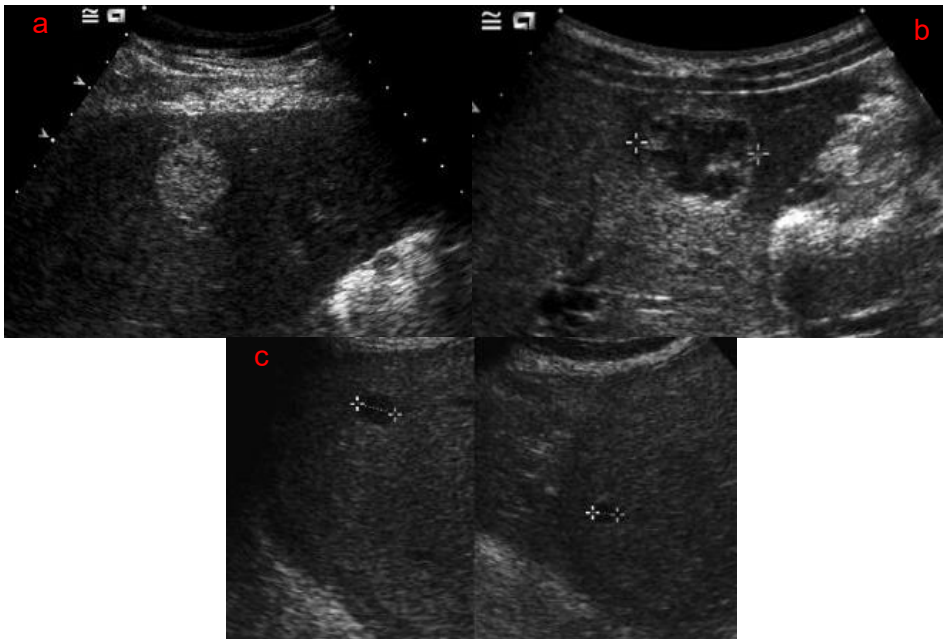

*Figure 7 - Different examples of metastasis sonographic appearances: **a** - Hyperechoic with hypoechoic halo; **b** - Hypoechoic with hyperechoic halo (rare); **c** - Small hypoechoic lesions.*[13]

2.2. *Image Guided Radiation Therapy*

Radiotherapy is, generally, a local or loco-regional treatment that focuses on directing the radiation to the tumor target while minimizing, as much as possible, the dose to surrounding normal tissues [15], [16]. For this purpose, a treatment plan must be elaborated, prior to the treatment, based on patient specific anatomy and physical density, usually provided by a Computed Tomography (CT) scan, which provides density information for dose calculation. On this CT scan image, the surrounding tissues and target volumes will be delineated [16, 17].

Tumor and organ motion often difficult the treatment delivery process [18]. Tumors located in organs like lung, pancreas, liver, prostate and breast move significantly due to reasons such as respiratory and cardiac motion, volume variations in surrounding organs (e.g., bladder or intestinal filling), tumor growth or shrinkage, tissue swelling and patient setup errors, leading to inter and intra-fractional uncertainties [19].

Inter-fractional changes accounts for variations between interval treatment sessions, while intra-fraction motion relates for organ or tumor movements that may occur during the treatment session [20]. Typical variations in liver motion due to breathing range between 5 mm to 35 mm, with most of the changes occurring in the Superior-Inferior direction (SI), followed by the Anterior-Posterior (AP) direction [21]. These result in significant geometric and dosimetric uncertainties in the therapeutic dose delivery. To accommodate for such errors and to ensure appropriate coverage of the target volume, geometric safety margins can be applied. On the other hand, the use of large margins also increases dose to the surrounding healthy tissues, the so called Organs-At-Risk (OAR) [22].

The introduction of IGRT has improved the accuracy of radiation therapy by providing imaging registration based on anatomic information, which allows for the application of tighter safety margins and therefore better healthy tissue sparing [6, 16]. Different imaging systems have been used to determine the position of the contoured volumes of interest (OAR and target) at the treatment stage. Some may only be used immediately before treatment delivery (accounting only for inter-fractional motion) while others provide monitoring during the whole treatment (correcting for intra-fractional uncertainties). Among these systems, there are well established techniques such as X-ray imaging, in-room Cone-Beam Computed Tomography (CBCT), implantation of FM, Electromagnetic (EM) beacons, Optical Surface Monitoring Systems and US imaging [15–17, 19, 21, 23]. The advantages and disadvantages of these modalities are summarized in *Table 1* and will be further developed on the following paragraphs.

Table 1 - Summarized IGRT modalities. ADVANTAGES highlighted in green, DISADVANTAGES in red.

	X-Ray			Optical	EM	FM	US	
	Planar	Fluoroscopy	CBCT				Manual	Robotic
Ionizing	Yes	Yes	Yes	No	No	No	No	No
3D/Volumetric	No	No	Yes	No	No	No	Yes	Yes
Bony Anatomy	Yes	Yes	Yes	No	No	No	No	No
Soft Tissue	No	No	Yes	No	No	No	Yes	Yes
Real-time	No	Yes	No	Yes	Yes	Yes	No	Yes
Surface	No	No	Yes	Yes	No	No	No	No

2.2.1. X-ray imaging

These are the most commonly used IGRT tools. These methods can use the Mega-voltage (MV) treatment beam or a dedicated diagnostic x-ray tube and detector. Although useful and widely used all these techniques require the administration of extra ionizing radiation to the patient.

Using either the MV beam or the dedicated Kilo-voltage (kV), X-ray tube planar images may be acquired, providing information on bony anatomy or surgically implanted fiducial markers [15, 17, 24]. This modality has several limitations: Imaging can only be performed before treatment, therefore not correlating motion during treatment; and bony structures do not always correlate to soft tissue and/or tumor position [6, 17, 25].

Another use for kV X-ray tubes is fluoroscopic imaging which allow for pre and during treatment imaging. Fluoroscopy allows only for detection of high density structures, such as bone, calcifications, fiducial implants and/or high tumor densities [17, 25, 26].

CBCT, on the other hand, relies on the rotation capability of the linear accelerator to acquire volumetric kV images of a certain Region of Interest (ROI) providing sufficient soft tissue resolution to allow for a three-dimensional (3D) location and shape of the target and surrounding organs. Being, so far, the only X-ray modality capable of providing soft tissue information, CBCT is presently used as state-of-the-art pre-treatment setup correction. However, it is not usable during treatment administration [6, 15, 17, 23].

2.2.2. Electromagnetic Tracking

Electromagnetic tracking systems provide real-time uninterrupted motion monitoring for targets that may have significant motion. Usually, the electromagnetic antenna or transponders are implanted inside the target or attached to it. They are intended as a stand-alone unit and require no additional modalities such as x-rays for determining the position of the implant and target [27]. Such systems have been proven to be highly accurate in detecting organ motion and are non-ionizing; however, they do not provide information about the target itself or the state and position of the OAR. Also, they are site specific and can only be used for a limited amount of locations [27, 28].

2.2.3. Optical Systems

Such systems usually resort to the use of speckle projection photogrammetry approaches, laser cameras or infra-red surface markers for the detection of the patient surface. Studies show a high degree of precision in patient set-up in external beam radiation therapy [22, 29–31]. These techniques have great utility for real-time external motion monitoring and set-up correction, however, they do not correlate for internal organ motion and are, therefore, of more particular relevance when applied to targets located close to the skin and the subcutaneous tissues (e.g. breast irradiation) [32].

2.2.4. Fiducial Markers

Although CBCT introduced the possibility of in room acquisition of volumetric images providing great skeletal and soft tissue contrast, this imaging modality does not provide sufficient soft tissue information for all tumor sites. This is a major problem on abdominal and, sometimes, pelvic regions, where organs are substantially affected by inter and intra-fractional motion [6]. In order to overcome this limitation, at many institutions three to four gold FM are implanted in the periphery of the tumor, previously to the planning CT image acquisition [5, 33]. These markers may help to reproduce the position during treatment and could therefore be used as surrogates for motion monitoring [4, 25]. These may also be used by x-ray motion

management applications, that are able to visualize fiducial markers implanted around the tumor for real-time tracking during the entire treatment [34].

However useful, FM implantation requires a surgical procedure which has associated complications related with pain, bleeding and fiducial migration. Also, being metallic, markers produce severe artifacts when used with CT and Magnetic Resonance Imaging (MRI) and standing alone provide no volume or soft tissue information [5].

2.2.5. US Imaging

US imaging offers a possible alternative to the previously described approaches for imaging targets outside the skull and lung [7]. It enables rapidly developing two-dimensional (2D), three-dimensional (3D) and four-dimensional (4D) anatomical and functional imaging capabilities for inter-fraction and intra-fraction imaging [16]. It is relatively inexpensive and easy to use, and it can have a diagnostic value comparable to MRI or CT imaging. Plus, this modality is non-ionizing and provides real-time volumetric imaging with excellent soft-tissue contrast. Recently, real-time US imaging in 3D was developed. With continuous scanning over time, 4D monitoring of tissues during treatment is possible [35]. This enables real-time automated structure segmentation and motion compensation during treatment, facilitating adaptive treatment correction [8].

US IGRT systems can be divided in two categories: inter-modality and intra-modality systems. Inter-modality systems compare the contours of a different modality reference image (i.e. CT or MRI), acquired prior to treatment planning (simulation stage), to US images acquired at the treatment moment. The intra-modality approach compares the treatment US image with a reference US image acquired at the time of simulation [16, 36].

The first widely adopted inter-modality and inter-fractional US systems for IGRT were the B-Mode Acquisition and Targeting (BAT) system (NOMOS Corp., Cranberry Township, PA), and the SonArray system (Varian Medical Systems, Palo Alto, CA) [37–41]. These systems use a 2D diagnostic US imaging and an optical or mechanical means for tracking the position of the US probe with respect to the radiotherapy treatment delivery machine (Linear Accelerator – LINAC). In both, the patient is positioned with respect to the LINAC prior to beam delivery by matching the planning CT volume to US images spatially localized in the LINAC frame [7].

Several studies have compared BAT and SonArray positioning accuracy with X-ray FM positioning [30, 33, 34]. Although initial studies regarding the BAT and SonArray systems demonstrated the promise of improved soft tissue-based prostate positioning, cross-examination with X-ray fiducial imaging revealed systematic biases. These biases are partially due to the reliance on inter-modality matching of US and CT image information. For example, prostate volumes derived from CT scans are consistently larger than those derived from US images because of differing physical image contrast mechanisms and the inability of CT to differentiate structures accurately at low contrast [7, 10, 38].

A comparison of intra-modality US imaging and CT scans showed no significant differences in any direction, based on this, it was concluded that intra-modality-based positioning is more accurate than inter-modality positioning. Therefore, intra-modality image matching has been recommended to minimize patient positioning error in US-guided radiotherapy [44].

The Clarity System (Elekta AB, Stockholm, Sweden) is an inter-fractional system that leverages intra-

modality image matching instead of the inter-modality matching technique used by BAT and SonArray [35]. Since intra-modality image matching has been shown to improve accuracy over inter-modality matching, as mentioned before, the Clarity system should theoretically position patients more accurately than the BAT system or SonArray system.

Although better than inter-modality systems, conducted studies have shown some concerning results regarding Clarity's accuracy due to its inter-fractional approach, highlighting the disadvantages of such US image guidance systems [7, 39, 42, 43]. These include:

- Anatomy deformations caused by pressure applied by the US transducer on the patient's body. Since pressure applied during pre-treatment imaging is not present during beam delivery systematic positioning errors are common [45].
- Variability caused by the operator skill and level of training of freehand US-based patient alignment [16].
- Both Clarity and BAT systems rely on freehand probe manipulation, which would pose an unacceptable hazard to the probe operator if performed during treatment delivery. Thus, no imaging is available during beam delivery when accurate target tracking is most critical.

Given the disadvantages of inter-fractional systems described above, it becomes clear that Intra-fractional US guidance systems are the next step in the evolution of US imaging for radiotherapy, providing real-time, volumetric, markerless target tracking [7]. The foundation of an intra-fractional US guidance system is the utilization of a hardware device to maintain the US probe in imaging position during therapy while the staff is outside the treatment room, safe and protected from radiation exposure. It must hold the probe in a way that maintains the therapy target within the US imaging Field of View (FOV) throughout treatment while minimizing possible interference with the LINAC, the patient's body, and treatment beams.

2.2.6. Static Devices

The Clarity Autoscan System (Elekta AB, Stockholm, Sweden) was the first system capable of intra-fractional imaging. The Clarity Autoscan is built upon the original Clarity System, replacing the 2D US imaging system with a mechanical "wobbler" 3D/4D US probe and adding a hardware fixture for hands-free transperineal prostate imaging. The hardware is a simple, manually-operated 5 DOF fixture that is mounted to a plate on the treatment couch between the patient's legs, fixating the US probe into imaging, thus freeing the staff to exit the treatment room during treatment delivery. The 3D/4D probe enables volumetric US images to be automatically captured without physically moving the US probe head.

Clinical studies of the system are underway to characterize the performance of the Clarity Autoscan system for intra-fractional monitoring [35, 39].

2.2.7. Robotic Devices

Stanford Prostate and Abdominal Imaging Robots

Schlosser, *et al.* [46] were the first to demonstrate the feasibility of robotic intra-fractional US imaging in the context of radiotherapy guidance. The authors developed and evaluated a robotic device designed for controlling 2D transabdominal US imaging of the prostate, demonstrating that gantry collisions are avoidable, that stable remotely-controlled prostate imaging is achievable in healthy human subjects over 10-minute time periods, and that robotic performance is not degraded during operation of a 15 MV radiation beam.

A second-generation custom-designed robotic device based on learnings from the previously described prototype was then developed by Wester, *et al* [7]. The goal of the research effort is to produce a simple, compact, human-safe robotic design that enables 3D/4D US imaging of any abdominal radiotherapy target, actively controls probe force, allows rapid and repeatable positioning of the US probe, and eliminates metal in areas exposed to CT/therapy radiation.

The robot has demonstrated successful imaging over extended time periods on the prostate, pancreas, liver, and kidneys of healthy volunteers under informed consent.

Johns Hopkins Abdominal Imaging Robot

Sen, *et al.* [47] have developed a custom-designed robotic manipulator for US-guided radiotherapy, focusing on overcoming inconsistencies in tumor localization between the planning and treatment phases due to tissue deformation induced by probe pressure.

In *ex vivo* experiments using a bovine liver fixed in gelatin with implanted fiducials, the system demonstrated repeatable arm placement with minimal effect on displacement of the fiducials. Later, in vivo experiments conducted on a dog demonstrated mean 3D reproducibility of 0.6 to 0.7 mm, 0.3 to 0.6 mm, and 1.1 to 1.6 mm for the prostate, liver, and pancreas, respectively, under position control and controlled ventilation [48].

Force control proved to be less reproducible however, indicating that position control rather than force control should be used for robotic substitution of real and model probes. Results indicated that the system shows promise for monitoring real-time organ motion, particularly under conditions of minimal probe pressure.

University of Lubeck Robotic Platform

The University of Lubeck has developed a robotic US probe positioning system for CyberKnife™ radiotherapy using an off-the-shelf robotic arm (Viper S850, Adept Technology, Inc.) [49]. The robot has six actively-controlled DoF, enabling probe placement on nearly any part of the patient's body. Continuous high-quality imaging was confirmed by showing that image structure/entropy stayed above the threshold for continuous target tracking of heart volumes at least 95% of the time in three healthy human subjects over 30-minute time intervals [49]. An updated version of the system uses a KUKA (Augsburg, Germany) 7-axis lightweight robot with integrated force control. In addition to manual 6-DoF positioning, force and image-based positioning strategies have been developed.

2.3. *Automatic Tissue Tracking*

All the systems previously described aim at intra-fractional treatment intervention. However, none of that would be possible without imaging methods capable of processing the acquired US images in real-time in order to extract soft-tissue motion information. Some studies have already been developed to assess the feasibility of tissue tracking algorithms for both 2D and 3D/4D US imaging.

Schlosser *et al.* conducted two different studies regarding the application of 2D US in monitoring soft tissue displacement [7, 50]. Both demonstrated that 2D US monitoring for displacement of internal features is feasible and even superior than tracking of an external surrogate [7].

Several different studies were carried out regarding the application and feasibility of 3D/4D US tissue tracking algorithms [50–55]. Generally, all proved that such algorithms are reliable and applicable.

Kubota, et al. studied the application of such algorithms for monitoring organs affected by respiratory motion. This proved to be feasible with an average tracking accuracy of 1.54 ± 0.9 mm (accuracy being defined as deviation from the center of the region of interest and the center of the target) [52].

Bruder, *et al.* proved the successful employment of an algorithm based on the matching of a current US volume and a template [56].

Some studies were specifically applied to the evaluation of accuracy and precision of real-time 4D US tracking on liver motion [53, 55, 57]. For instance, Harris *et al.* used a mechanically swept probe on both a tissue-mimicking phantom and on *in vivo* liver motion of healthy volunteers: for phantom-based experiments, accuracy and precision (Root Mean Square [RMS] error and Standard Deviation [SD]) were found to be 0.78 mm and 0.54 mm, respectively; for *in vivo* measurements, mean absolute distance and standard deviation of the difference between automatically and manually tracked displacements were less than 1.7 mm and 1 mm, respectively, in all directions (left–right, anterior– posterior and superior–inferior). Good agreement between automatically and manually tracked displacements indicates that 4D ultrasound-based motion tracking has potential for image guidance applications in radiotherapy [7, 55].

2.4. *Image Registration and Spatial Transformations*

Image registration is the process by which two images are aligned, transforming different data sets into one coordinate system. In other words, it is the process of determining the correspondence between two different images (acquired in different moments in time, from a different angle or with different conditions), typically between the reference image (fixed) and the target image (moving), and recovering the geometrical or spatial transformation that aligns both images[58-60].

A spatial transform ($\mathbf{U}$) plays the role of representing registration solutions in a precise manner, describing a mapping between the coordinate system of one image and that of another image.

There are several terminologies that refer to different properties of $\mathbf{U}$ [60, 61]:

Smoothness – A mapping $\mathbf{U}$ is said to be smooth if all of its partial derivatives of a certain order exist and are continuous. Properties of $\mathbf{U}$ affect the appearance of the image to which it is applied. Generally, this property is desired as it directly affects the smoothness of the image on which it is applied.

Bijectivity – $\mathbf{U}$ is said to be bijective if it consists in a one-to-one mapping. Bijectivity ensures that

the folding of a space does not happen as multiple points cannot be mapped into the same point. Depending on the application, this property, may or may not be required.

Invertibility – $\mathbf{U}$ is said to be invertible (or homeomorphic, or topology-preserving), if it is bijective and continuous (and its inverse also).

When $\mathbf{U}$ is both smooth and invertible, it is called **diffeomorphic**. A diffeomorphic transform is required when one needs to maintain the connectivity between neighboring anatomical structures after registration.

In order to parametrize $\mathbf{U}$, spatial transformation models (transforms) are often used. The ones commonly used for image registration are categorized as either **linear** or **nonlinear** and they differ in terms of their DoF, which in turn determine the different types of geometric distortions that they induce on images [59–62].

Linear transforms – Include translation, rotation, rigid, affine and projective. A rigid transform allows for translations and rotations only; an affine transform allows for rigid as well as scale and shear (distortions that preserve parallelism of lines); a projective transform allows for all distortions that preserve collinearity (lines remain straight after distortion).

Nonlinear transforms – Allow for more localized deformations. These transformations are capable of locally warping the target image to align with the reference image – mapping curves to lines. In general, these can be divided into two categories:

- Physical models - Derived from the theory of continuum mechanics (elasticity, optical flow and fluid flow).
- Function representations – Originate from interpolation and approximation theory, using basis function expansions to model the deformation (radial basis functions, *B*-splines and wavelets).

2.5. *Image registration algorithms*

An image registration algorithm consists in four main components: the source of information (feature or intensity based), the similarity measure, the optimization method and the transformation model [58].

Regarding the source of information there are two main approaches: feature-based and intensity-based. Feature-based image registration extracts a set of geometrical features from one image and looks for the corresponding on a second one. These features include corners, landmarks, line segment curves and surfaces. In medical applications this features may represent distinct anatomical regions or FM. One advantage of feature-based methods is their low computational load – after identifying the geometrical features, image intensities are no longer required for the registration process. One disadvantage of these methods is that they rely on successful feature identification and extraction and require a long pre-processing step [58, 63, 64].

Intensity-based image registration aligns images directly based on their intensities and has recently become the most widely used registration basis for several applications. The available intensity information at each voxel allows for more accurate estimation of local non-rigid deformations and allows for registrations taking into account all the available image information. In its simplest form, the registration transformation is determined by iteratively optimizing a similarity measure calculated from all voxel values [58, 62, 65].

Similarity measure is usually an objective function that reaches a *plateau* when two images verify a certain relationship. Examples of popular similarity measures are the mean square differences, sum-of-squared-differences or mutual information [66].

The optimization method is an algorithm to find a set of parameters that optimize a given similarity measure. Standard optimization methods are often employed including Gradient Descent, Quasi-newton, Stochastic Gradient Descent or Evolutionary methods [65, 66].

Finally there is the need to consider the transformation model, responsible for defining the way to deform the image sets. These are typically divided into two large groups: rigid or non-rigid. Rigid mappings may be defined as geometrical transformations that preserve all distances, the straightness of lines and all nonzero angles between straight lines. This type of transformation is always global as the resulting transformations are equally applied to the whole image. The most simple and common transformation model is rigid (allows translation and rotation). Another global transformation type is the affine, which allows for scaling and shearing. The shearing capabilities of the affine model make it a non-rigid transformation however, due to its simplicity and linear preserving characteristics, affine is often considered as rigid. Other examples of more complex non-rigid transformation models are basis function expansions (ex: radial basis functions or *B*-splines) or derived from the theory of continuum mechanics, such as elasticity or optical flow. These models are able to map straight lines to curves and locally warping the target image to align with the reference image [58–61, 63, 64, 67].

3. Implementation

3.1. *Experiment Outline*

The original objective of this study was to create a tool that would possibly solve the disadvantages inherent to the use of FM by developing an image-guided robotic system that could be used for both FM implantation and the tracking of these same fiducials during treatment. However, after an extensive literature review there was the realization that a properly developed 3D ultrasound image-guided robotic approach would possibly be capable of overcoming the need for the use of FM allowing for direct 3D tracking of the tumor or tissue, leading to the consequent adjustment of the primary goal. The development staging and methodologies outlined for the updated approach are:

1. Construction of a realistic 4D-liver model phantom.
2. Development of a MATLAB application capable of co-registration of 3D US imaging onto a reference US scan from a region of interest (phantom).
3. Development of an application capable of performing semi-automatic registration of 3D US images and defined density identification in order to monitor tumor motion.
4. Analytical assessment of the organ tracking system precision.

3.2. *4D Liver Phantom*

In order to successfully achieve the proposed goal, adequate images of the anatomical ROI needed to be acquired, either from a live voluntary or from a realistic anatomical model of the ROI.

Considering the possibility that, during the development of the US image registration application, the author would need to make multiple tests with different acquisition types, the usage of a live voluntary would create great difficulties due to availability and variability. Also, the existence of an identifiable liver lesion was mandatory and thus the voluntary would necessarily have to be someone with a medically diagnosed liver tumor, which would create even greater complications.

Developing a proper anatomical model would ideally solve availability and variability issues. It would also allow the author to acquire images under controlled conditions, and with exact knowledge of lesion location and movement. Even though this was the selected method, it was required that the model would meet certain specifications in order to be as realistic as possible:

- Medium echogenicity consistent with human soft tissue
- Lesion echogenicity consistent with liver tumors
- Breathing alike movement and effect on adjacent tissue
- Tissue compression rate similar to the human tissue

In order to fulfill the requirements stated above, a first draft of the anatomical model, from now on referred to as phantom, was drawn comprising:

1. A homemade echogenic media simulating the liver soft tissue elastic behavior and imaging characteristics
2. Implanted homemade inserts to simulate US imaging characteristics of liver tumors.

3. An inflatable balloon that would simulate lung behavior - compressing the surrounding media when inflated and decompressing when deflated, causing the lesion to change in position and shape accordingly.
4. A device that would allow the user to pump air in and out into the balloon and the phantom.

After a process of research and experiments, a refinement was made to the original sketch, replacing:

1. The inflatable balloon by a test lung silicon bag (artificial lung), used for the calibration of pulmonary function tests equipment (*Figure 8*).

Figure 8 - Test lung silicon bag (artificial lung)

2. The air pump, by a Bi-level Positive Air Pressure (BiPAP) ventilator kindly donated by the Linde Group Inc., healthcare division (*Figure 9).*

Figure 9 - Bi-Level Positive Air Pressure (BiPAP) ventilator

This resulted in the first successfully achieved phantom, illustrated on the Figures 10 and 11.

Figure 10 - First phantom developed with a homemade echogenic medium.

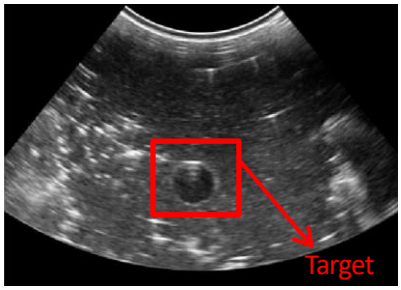

Figure 11 - Ultrasound image of a selected target (First Phantom)

Although this model was satisfactory for this experiment the biological and biodegradable components of the homemade echogenic medium suffered severe degradation over time which lead to its invalidation. Since building a new phantom every few days would add a large bias to the test images a different solution was pursued leading to the replacement of the homemade echogenic media and lesion inserts for US phantom specific material - a contribution from CIRS Inc., along with melting and manipulating instructions. These resulted in the final US test phantom schematized in *Figure 12* and illustrated on *Figures 13* and *14*.

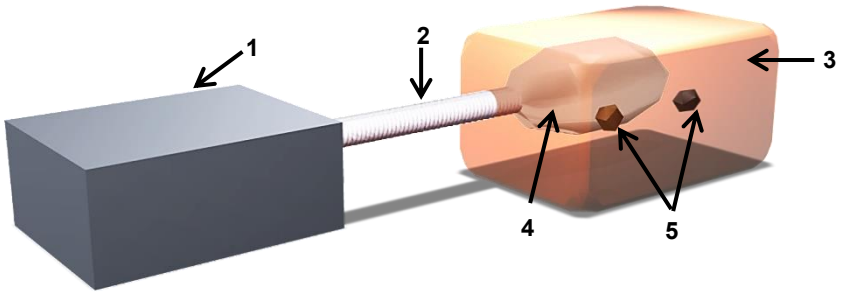

Figure 12 - 3D Schematic of the final Liver Phantom, where 1 is the Bi-PAP, 2 is the tube that carries air into the artificial lung, 3 is the soft tissue US medium, 4 is the artificial lung and 5 corresponds to liver lesions with appropriate echogenic behavior.

Figure 13 – Picture of the final liver phantom.

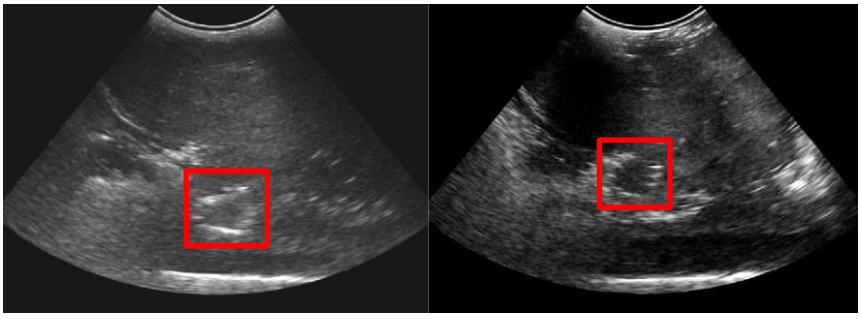

Figure 14 - Ultrasound image of the two targets inserted into the Liver Phantom. Targets highlighted with a red square.

The final Liver Phantom proved to be a long lasting and adequate solution to perform the necessary tests during the development of this project, checking all the conditions previously specified. Furthermore, at the moment of writing this document, it still preserves all the initial features which allows us to expect that it will endure overtime.

The targets/lesions inserted in this final phantom are slightly more difficult to identify, nevertheless this is consistent with the expected physiological response and therefore provide a more accurate testing model.

To facilitate the identification of the inserted lesions and also in order to add rigid features that would be accurately identified on all image acquisitions, one FM was implanted in the center of each lesion with the assistance of a specific needle and guided by the US image (*Figure 15*).

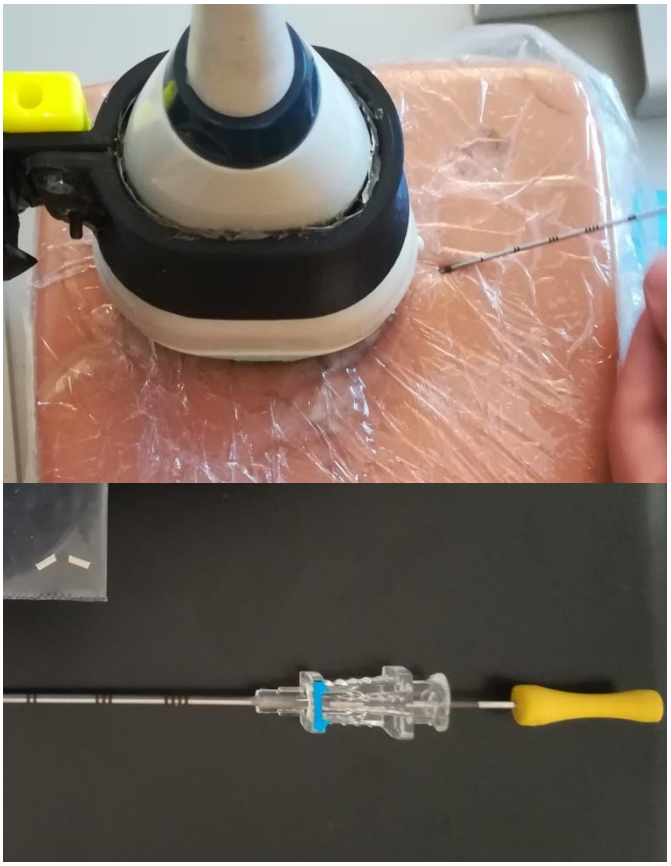

Figure 15 - FM implantation procedure (up). Close up on the FM and implantation needle (bottom).

The implanted FM are a polymer based product (PolyMark™), 1 mm wide and 3 mm long, specifically designed for IGRT applications, ensuring proper identification on all imaging modalities with minimal artifact (US, CT and MRI) and minimal tissue migration due to their spiral-cut surface. PolyMark™ FM and the implantation needle were generously provided by ABGT, Lda.

Developing this Liver Phantom was a large step in the successful implementation of the proposed approach. It was especially important due to the fact that, to the author's knowledge, there is no similar solution commercially available given that all US 4D phantoms available rely on mechanical systems, which will inherently behave less physiologically. By coupling a medical ventilator to the inflatable artificial lung, we not only assured a human like behavior but also gained the ability to adjust different values such has breathing frequency and amplitude. On the other hand, the elasticity of the material used for the medium assured that the inserted lung would be able to inflate and deflate causing the lesions to move and compress simultaneously changing in position and shape much like the functioning of the human body.

3.3. *US Acquisition System*

For this project, the available 3D Ultrasound system existing in the Surgical Robots Lab (SRL) was used, the Ultrasonix SonixTABLET (*Figure 16*). It consists in a computer with two dedicated ports for the insertion of US transducers and specific software for the visualization of the acquired images. Besides the usual Clinical Mode it also allows for operation under a Research Mode. Through a variety of Software Development Kits (SDK), direct access to the US images and to the acquisition parameters is granted to the user.

Figure 16 - The SonixTABLET ultrasound system

Propello was the chosen SDK for this project as it is specifically designed to manipulate 3D integrated transducers, communicating with the wobbling mechanism while US images are acquired, accessing the images from cine memory. Thanks to the two input and two output digital signal ports this open source software allows the triggering or the detection of an image acquisition, respectively. An output signal can be used to synchronize other devices to the image acquisition, namely, to retrieve the relative position of the ultrasound probe.

Additionally the 4DC7-3/40 Convex 4D US transducer was used (*Figure 17*). This transducer is specific for Abdominal, Gynecological and Pediatric applications and features a frequency range of 7 MHz to 3 MHz, a focal range of 5 cm to 24 cm and a 79º image field.

Figure 17 - The 4DC7-3/40 Convex 4D ultrasound transducer

3.4. *Kuka Lightweight Robot*

Born from a partnership between Kuka Robotor Gmbh and the Institute of Robotics and Mechatronics of the German Aerospace Center (DLR) the KUKA Lightweight Robot (LWR) belongs to a revolutionary generation of robots whose applicability is mostly related with aiding and assisting humans in general tasks either at home, office or public spaces such as hospitals.

This LWR is a seven degrees-of-freedom (DoF) robotic arm with flexibility to work in cluttered and unstructured workspaces where there is little information about the surrounding environment (*Figure 18*). One of the DoF is redundant and helps avoiding typical singularities of 6-axis kinematic systems[68]. Furthermore it makes it reconfigurable while holding the pose of the end effector. Integrated force torque sensors allow for hands on cooperative control including impedance control and virtual fixtures [69].

Figure 18 - KUKA LWR with controller and KUKA control panel (KCP.) [70]

The designation of “lightweight robot” comes from the fact that the weight was severely reduced to the limits of what is technically possible, unlike previous generations of robots whose high position accuracy requires high stiffness at the cost of high robot mass relative to its payload. The low mass has consequences such as decisively improving robot’s dynamic performance and reducing power consumption. Having a mass of 16 kg, the KUKA LWR is designed to handle up to 7 kg at low velocities [68, 69].

KUKA LWR can work on gravitic compensation, joint position control or joint and Cartesian impedance control. As such, it is suitable for accurate positioning, but also for more compliant interaction with the user, making it an interesting device for the field of robot assisted surgery and image guided applications. As the arm already provides the required compliance for additional tools an ultrasound probe can be mounted on the robot’s end-effector and be used for medical image acquisition, where the medical staff has the ability to move the attached ultrasound freely as the robotic arm tracks and fine tunes its position. Tracking the pose of the probe for the acquired images is important for the volume reconstruction of the 3D US scan and determine its position in order to accurately allow for shift estimation between two different volumes [68–70].

3.5. *NDI Polaris Spectra*

The Polaris® optical tracking solution provides exceptionally accurate and reliable 3D tracking of simulated medical tools (via attached markers) over a large measurement volume. The Polaris emits infrared light to wirelessly detect and track a tool's position and orientation in all six DoF. The position and orientation of each medical tool is tracked and displayed within the simulation software in real time. Data integration occurs seamlessly and instantly, providing uninterrupted tool interaction [71].

The goal of optical measurement is to calculate the location and orientation of an object or tool within a defined coordinate system, using a position sensor to detect infrared-emitting or retro-reflective markers affixed to a tool or object. The position sensor calculates the position and orientation of the tool based on the information the position sensor receives from those markers [72, 73].

NDI Polaris Spectra uses optical measurement and is integrated into medical solutions that have been widely adopted for use in computer-assisted therapy applications covering a broad spectrum including implant placement, ergonomic studies, neurosurgery and radiation therapy. For example, using a specially marked imaging device, such as an ultrasound probe, to locate the tumour would allow the ultrasound probe to be tracked by the Polaris Spectra Position Sensor, resulting in the ability to identify the exact location and orientation of the ultrasound probe [74].

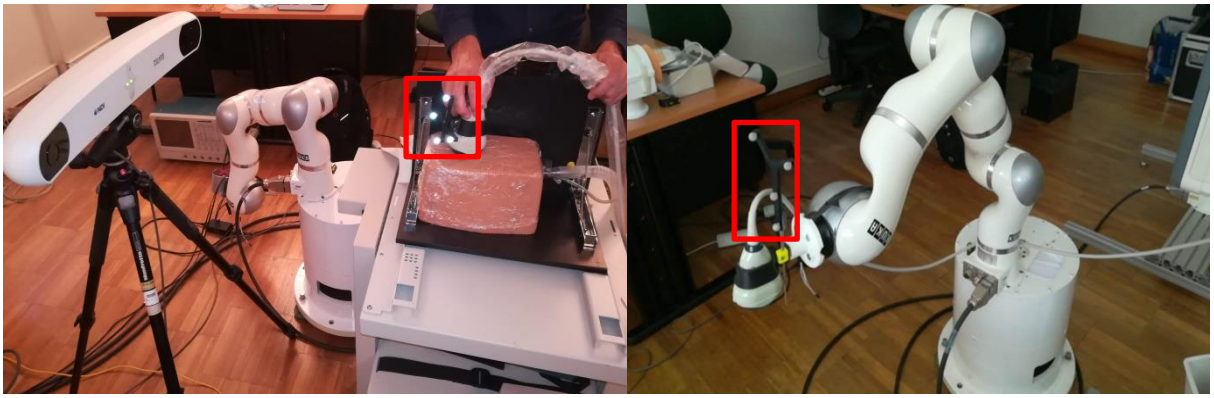

Figure 19 - Polaris tool set-up for two different applications: Step 1 on the left and Step 2 on the right. Infrared reflective markers highlighted in red.

For this particular application, Polaris was used for two different purposes, on different development steps as depicted on *Figure 19*. On a first period, it was used to acknowledge the position of the US probe during free-hand manipulation in order to acquire the first set of images for testing and optimization of the image registration algorithms. On a second phase, it was used to calibrate the assembling of the ultrasound probe to the KUKA's LWR end-effector and define the probe's position in the robots' reference frame.

3.6. *Integrated System*

The following steps describe the communication setup between all the hardware components previously described, Figure 20 is a schematic representation of the described protocol:

1. A MATLAB program running on the host computer commands the US image acquisition system to start the acquisition of a number of volumes through TCP;
2. Running simultaneously on the host, a Simulink program reads the poses from the Polaris optical tracking system and sends it to the target PC – in this case only required for free-hand probe manipulation and calibration of the US probe to KUKA's spatial referential;
3. The US system enables the output trigger port and commands the wobbler of the probe to the end of its FOV and then starts acquiring images and stepping the motor;
4. At the end of each image acquired, the image is sent through TCP back to the host and simultaneously an output trigger is sent from the SonixTablet BNC port to the data acquisition board on the KUKA Target PC;
5. On the KUKA Target PC, for each trigger detected, the current pose of the KUKA LWR end-effector is sent to the host computer through User Datagram Protocol (UDP). In case Polaris is being used, the poses acquired by the optical tracking system are also sent back to the host;
6. The host computer associates each image to the pose sent by the KUKA and stores the information;
7. When all the requested images are sent, the US system stops the image acquisition and disables the output trigger port.

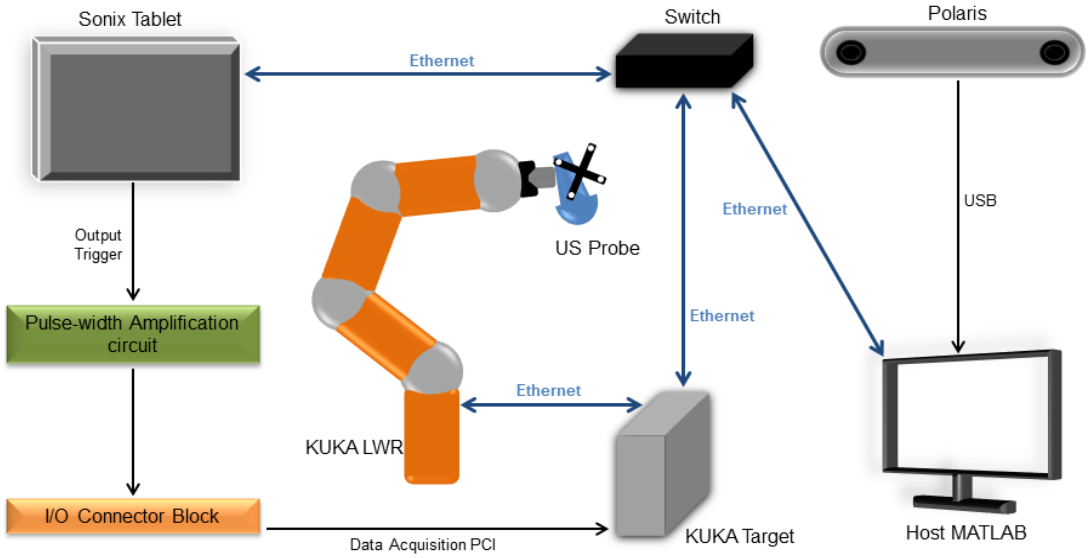

Figure 20 - Schematic of the Integrated System

Whenever the US system receives the command to acquire new images it stops all running acquisitions. At this moment, the output trigger port allows synchronization with external devices, in this case, the KUKA LWR. The motor position of the probe is set to one end of the defined FOV and the process of image acquisition begins, acquiring one frame and stepping the motor to the following position in a fan shape until the other end of the defined FOV. The overall path of all the motor steps corresponds to the acquired volume. The trigger output is disabled once the specified number of acquired volumes is achieved.

3.7. ***Robot-US probe holder***

In order to achieve a successful holder for robotic-guided US imaging acquisition system, the ultrasound probe must be attached to the robotic arm in a precise and safe manner. To achieve this assembly a coupling holder was designed using SolidWorks®, a sketch can be seen on *Figure 21*.

This holder would allow for the attachment of its base to the robotic arm and should also fasten to the already existing US probe hoop, as demonstrated on the right in *Figure 22*.

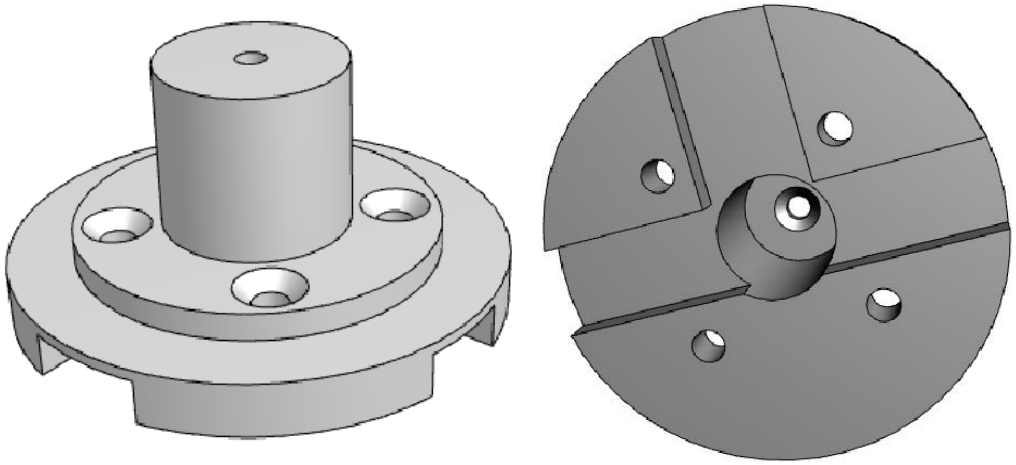

Figure 21 - 3D sketch of robot-US probe holder.

Figure 22 - Picture of the 3D printed holder and its assembly to the US probe hoop (on the right).

The manufacturing of this apparatus was accomplished via 3D printing using Polilactic Acid (PLA), well-known biodegradable polyester that has been widely used in medical applications.

With its low melting temperature (T_m) at approximately 180 ºC, PLA is easy to manipulate and to use in 3D printing applications being ideal for fast prototyping. It has proven appropriate for the experimental laboratorial framing of this project nevertheless, due its low glass transition temperature (T_g), at approximately 55 ºC, this thermoplastic material would present some limitations in a clinical setting such has the impossibility for high temperature sterilization, for example [75].

3.8. *3D Image Registration Tool*

MATLAB was the selected software to implement the proposed application. It already comprises several of the necessary functions such as image registration algorithms and 2D image fusion display. It does not include, however, any 3D image fusion display function, even though the existing image registration algorithms are suitable for 3D usage. Consequently, for the appropriate development and validation of the proposed application, an image registration tool needed to be developed encompassing manual upload of the reference and acquired image volumes (fixed and moving, respectively), image pairing and displaying in 3D, image cropping for user selected ROI definition, application of the implemented image registration algorithms, an option for manual image registration and visualization of the registration results. Lastly, a function was added in order to save the archived outcomes for each performed test. The final graphical appearance of the previously described tool can be seen in *Figure 23*.

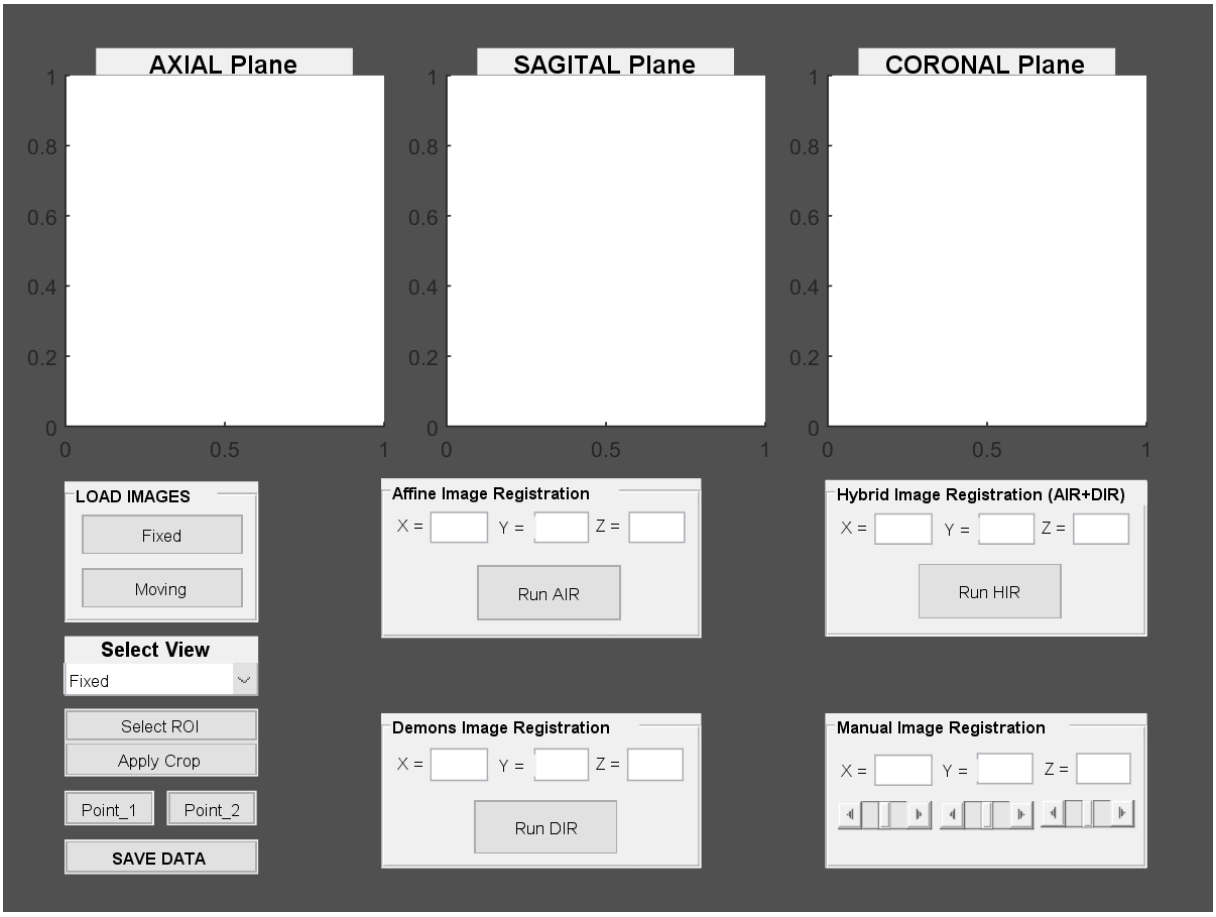

Figure 23 - Graphical appearance of the 3D image registration tool, developed in MATLAB.

On the following lines the developed tool will be further explained specially focusing on the image registration options and their fundamentals.

3.8.1. Loading images, view selection and ROI definition

On the bottom left side of the tool main window a few buttons are available, totally performing 4 different actions, as depicted in *Figure 24*. The user must begin by loading the fixed image (reference) and the moving image (target) from which it is desired to know the geometrical displacement in relation to the reference. On the second area (Select View), the user may alter between different views, given that the image has been uploaded and/or the function has been ran. Next, there is

an option to select and apply a ROI that, although not mandatory, will be useful to focus the registration to a smaller area encompassing the important features such as the lesion or target.

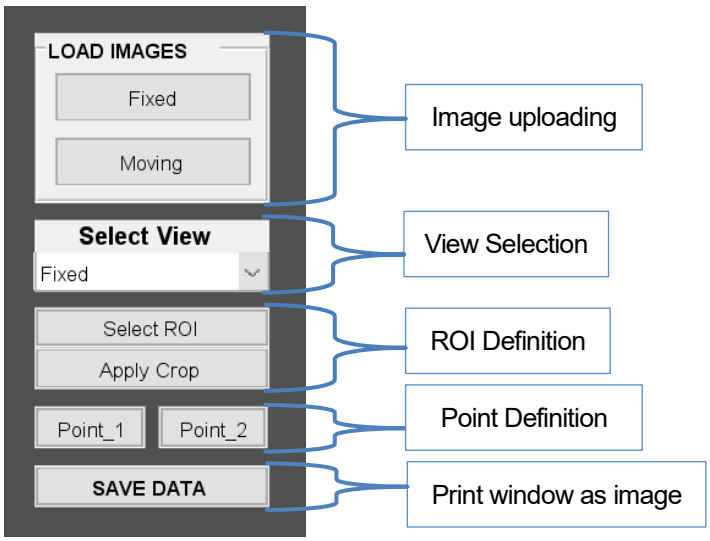

Figure 24 - Left bottom area, close up.

Following, two buttons were added to allow the user to select two points that conceptually would be located on the extremities of known fixed features on both image sets, more specifically, the fiducial markers approximately located at the center of each lesion. From these two opposite points the mean point of the FM is calculated and plotted in the corresponding image (*Figure 25*). Finally the user may save the achieved results by printing the window in display as an image.

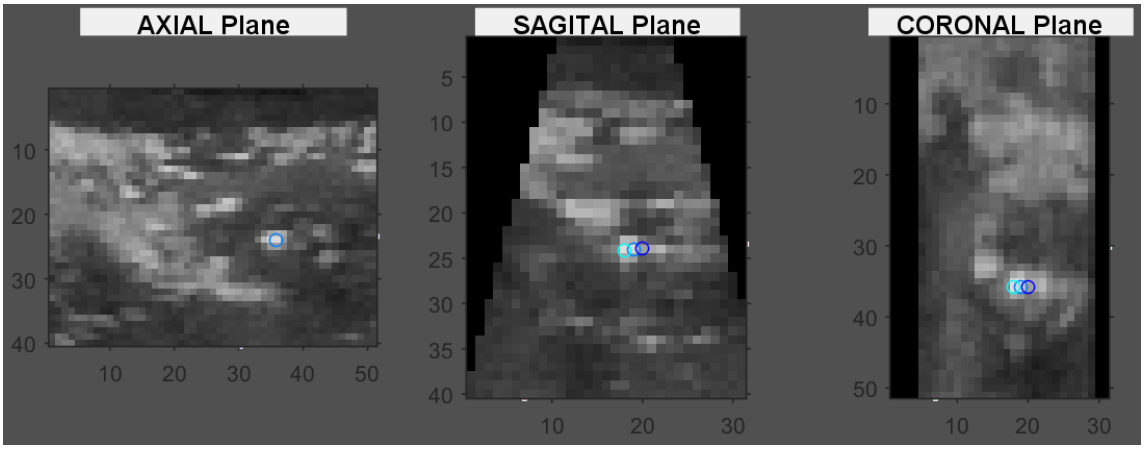

Figure 25 - Illustration of the CoM definition.

3.8.2. 3D Image visualization and pairing\fusion

On the upper area of the main window, lies the visualization region where images are displayed in 3 axis according to AXIAL, SAGITAL and CORONAL planes (*Figure 26*).

In this visualization area, the user might follow the registration process form image loading to image fusion and registration. Each option enables its own image display and automatically changes the view selection to the corresponding function. At the same time, if a function has already been ran, the user may also navigate through different images and outcomes by altering the selection view.

This visualization tool is responsible for the 3D image fusion function that is essential for the final

application that is proposed in this study. Based on the 2D imshowpair function already existing in MATLAB, each spatially referenced slice from the fixed image is paired with the corresponding referenced slice from the moving image.

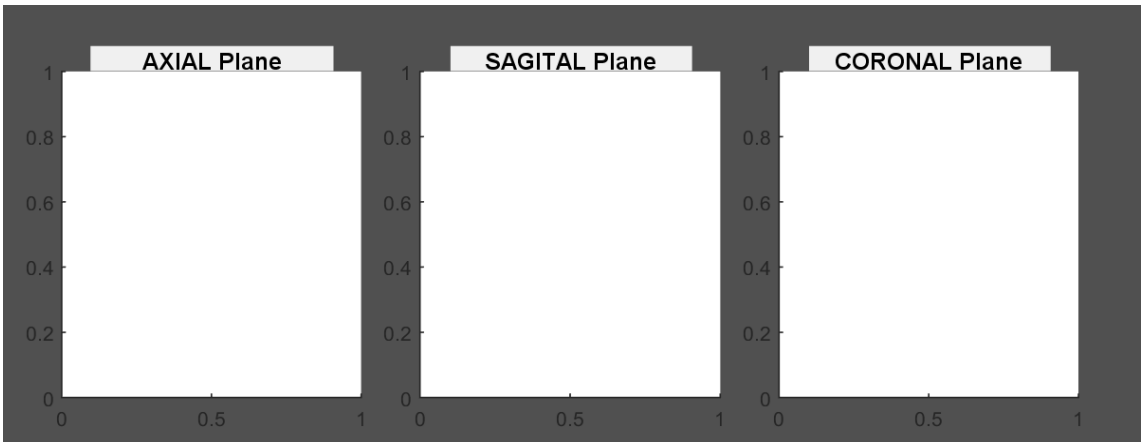

Figure 26 - Upper area, close up.

This allows the user to visually assess the error from image to the other and to evaluate the performance of each registration algorithm on all 3 planes (Axial, Sagittal and Coronal). A counter function associated to the image pairing function enables sweeping through the entire volumes by using the mouse scroll wheel. In areas where only one of the volumes exists, a function was developed to add a black colored slice to the pairing volume.

An example of the image fusion visualization can be found on *Figure 27*, also illustrating the graphical interaction enabled by the visualization area used, for instance, to select the ROI or to define the opposite points of the FM.

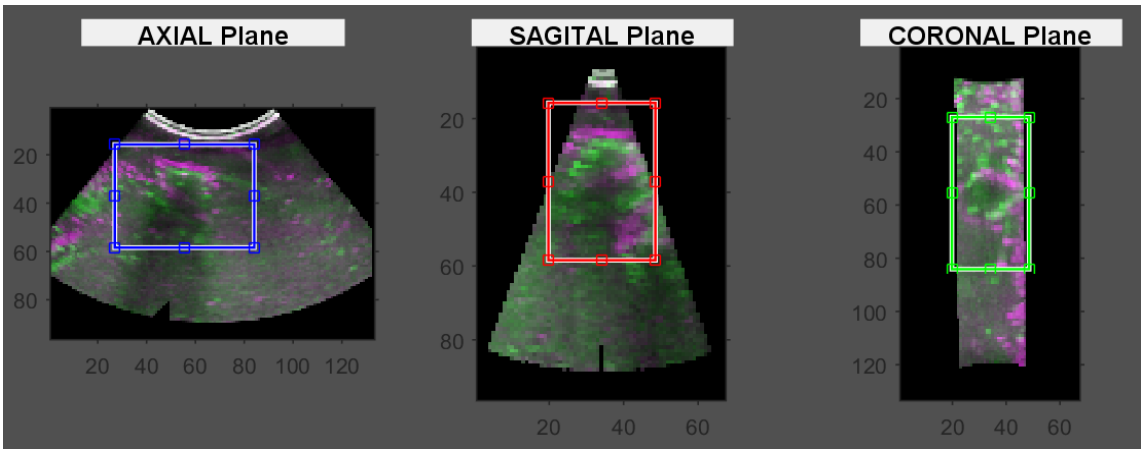

Figure 27 - 3D Image pairing and graphical interaction – ROI selection.

3.8.3. Image Registration Options

As for the image registration functionality of the developed tool, 4 options are available as shown in *Figure 28*.

From the available options, the Manual Image Registration (MIR) buttons allow the user to manually shift the position of the moving image in X, Y and Z directions. This option was added in order to be used as a metric reference to evaluate the performance of the implemented algorithms and also to compare manual registration to the other modalities. The remaining options are Affine Image Registration (AIR), consisting in an

affine transformation optimized for the image modality in use, Demons Image Registration (DIR) consisting in a demons algorithm and a Hybrid Image Registration (HIR) comprising a 2 step registration process that starts with an affine transformation followed by the DIR algorithm optimized to work sequentially.

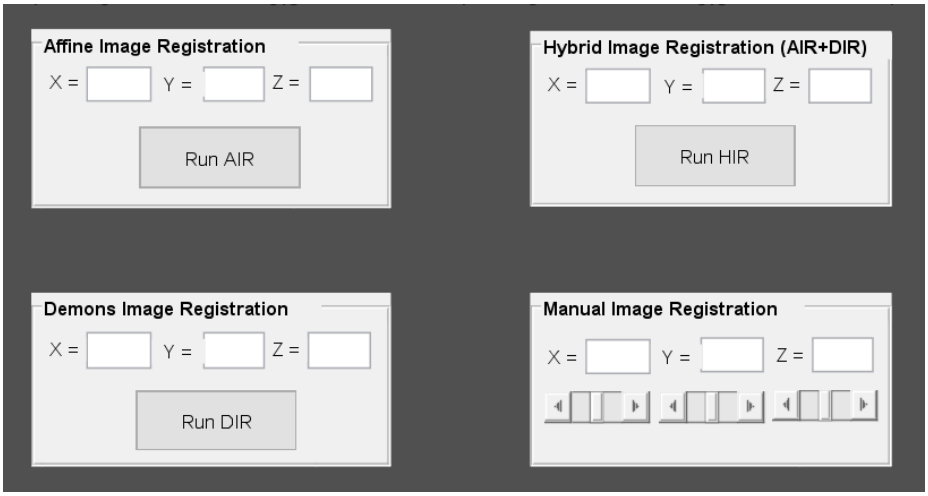

Figure 28 - Right bottom area, close up.

The two core algorithms underneath this application are the AIR and DIR. Further explanation of their functioning, principle and implementation follow bellow.

3.8.3.1. Affine Image Registration (AIR)

This function estimates the geometric transformation that aligns two 2D or 3D images using intensity based registration.

As previously explained, intensity-based automatic image registration is an iterative process. It requires the user to specify a pair of images, a metric, an optimizer, and a transformation type. The metric defines the image similarity metric for evaluating the accuracy of the registration. This image similarity metric takes two images and returns a scalar value that describes how similar the images are. The optimizer defines the methodology for minimizing or maximizing the similarity metric. The transformation type defines the type of transformation that brings the misaligned image (moving image) into alignment with the reference image (fixed image).

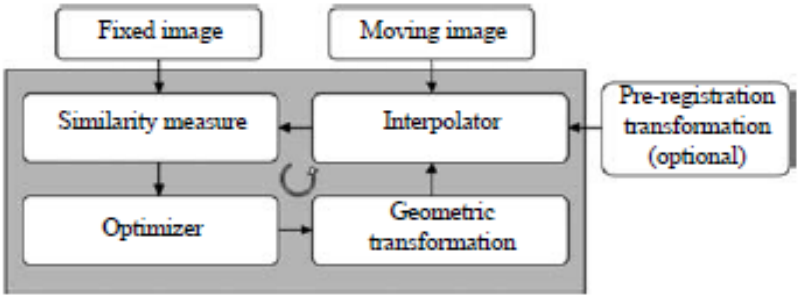

Figure 29 - Diagram of the typical algorithms used for intensity-based registration methodologies.[62]

The process begins with the transform type that has been specified and an internally determined transformation matrix. Together, they determine the specific image transformation that is applied to the moving image with bilinear interpolation.

Next, the metric compares the transformed moving image to the fixed image and a metric value is computed.

Finally, the optimizer checks for a stop condition, a point during the process where the error in one iteration or the error improvement between iterations is below a certain threshold or when the specified maximum number of iterations has been reached. If the stopping criterion is not met, the optimizer adjusts the transformation matrix to begin the next iteration. In this case, an affine transformation will be applied. This method has been used in the registration of ultrasound images since the low resolution and low signal-to-noise ratio of the ultrasound images make the accurate registration more difficult when more complex transformations are used. *Figure 29* demonstrates a typical algorithm used in intensity-based registration methodologies [62].

Implementation

For this registration method, MATLAB has two options available for both the optimizer and the similarity metric.

- **Optimizer:**
    - Regular Step Gradient Descent – this optimizer adjusts the transformation parameters so that the optimization follows the gradient of the image similarity metric in the direction of the extrema. It uses constant length steps along the gradient between computations until the gradient changes direction, then a bipartition scheme is used to compute the step size.
    - One Plus One Evolutionary – This optimizer follows the evolutionary theory simulating the biological evolution of a set of samples in the search space. Basically, it iterates to find a set of parameters that produce the best possible registration result by perturbing, or mutating, the parameters from the last iteration (the parent). If the new (child) parameters yield a better result, then the child becomes the new parent whose parameters are perturbed, perhaps more aggressively. If the parent yields a better result, it remains the parent and the next perturbation is less aggressive.
- **Metric:**
    - Mean Squares Metric - Computes the mean squared pixel-wise difference in intensity between to images over a region. Relies on the assumption that intensity representing homologous points must be the same in both images and any linear changes in the intensity result in a poor match value. It is often simple to compute and has a large capture radius.
    - Mutual Information – This metric measures how much information one random variable tells about another random variable (image intensity in both images). This information is a quantitative measure of how similar the images are. High mutual information implies a large reduction in the uncertainty between the two distributions, signaling that the images are likely better aligned.

As seen before and as displayed in *Table 2* there are a total of four possible combinations from which to optimize the algorithm. Initial tests were performed in order to estimate which combination

would perform better with the imaging modality at study. These tests pointed that combining the Regular Step Gradient Descent optimizer with the Mean Squares Metric resulted in more accurate image transformations. Graphical outcomes can be visualized and compared in *Figure 30*.

Table 2 - Affine algorithm combinations.

	Optimizer	Metric
Combination 1 (C1)	One Plus One Evolutionary	Mean Squares
Combination 2 (C2)	One Plus One Evolutionary	Mutual Information
Combination 3 (C3)	Regular Step Gradient Descent	Mean Squares
Combination 4 (C4)	Regular Step Gradient Descent	Mutual Information

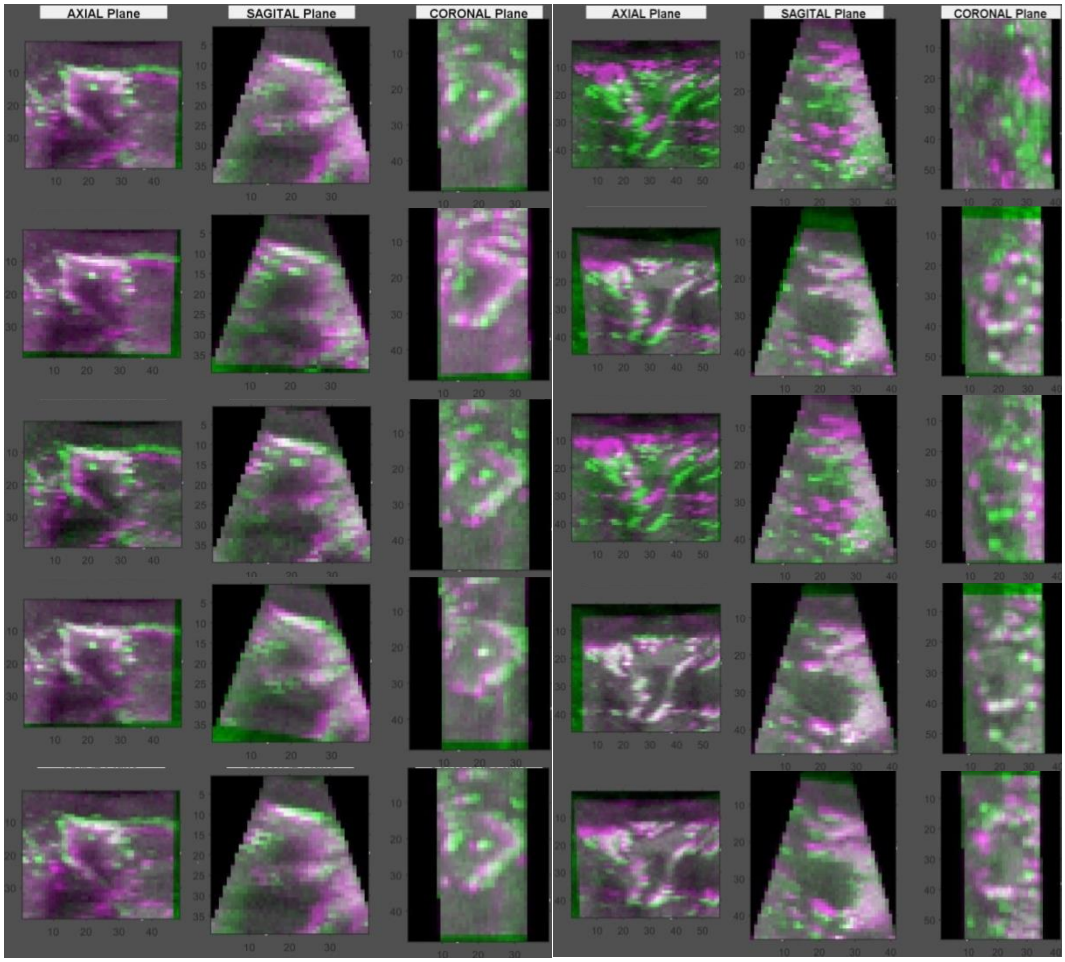

Figure 30 - Image registration comparison for different combinations, lesion 1(left) and lesion 2(right). From the top image to the bottom displayed images are: Image fusion without registration; Combination1; Combination2; Combination3; Combination4.

3.8.3.2. Demons Image Registration (DIR)

Demons algorithm is a type of optical-flow transform based on a diffusion process [62]. In this process, voxels are pushed into or out of object boundaries to allow for image matching, by treating images as isointensity contours and computing demon forces to push these contours in their normal direction to encourage image alignment [60].

Demons algorithm preforms exceptionally fast, and is very efficient on real 3D data [76]. The method uses an approximate elastic regularizer to solve an optical flow problem, where the “moving” images level sets are

brought into correspondence with those of a reference or “fixed” template image [77].

A disadvantage of this model is that there are no constraints on the displacement and it does not necessarily preserve the topology. In practice, the algorithm computes an optical flow term which is added to the total displacement (initially zero). To reduce the effects of noise, the accumulated displacement field is then smoothed by Gaussian convolution. The algorithm iterates over time, during each iteration an incremental displacement field is determined and the source image is resampled for the next iteration [59].

As a non-parametric method, the implementation of demons algorithm is relatively simple, in the way that only a few parts of the process might be optimized, more precisely the number of multi resolution pyramid levels, the number of iterations performed at each pyramid levels, and the amount of diffusion-like regularization that is applied to the standard deviation of the Gaussian smoothing to regularize the accumulated field at each iteration - smaller values result in more localized deformation in the output displacement field.

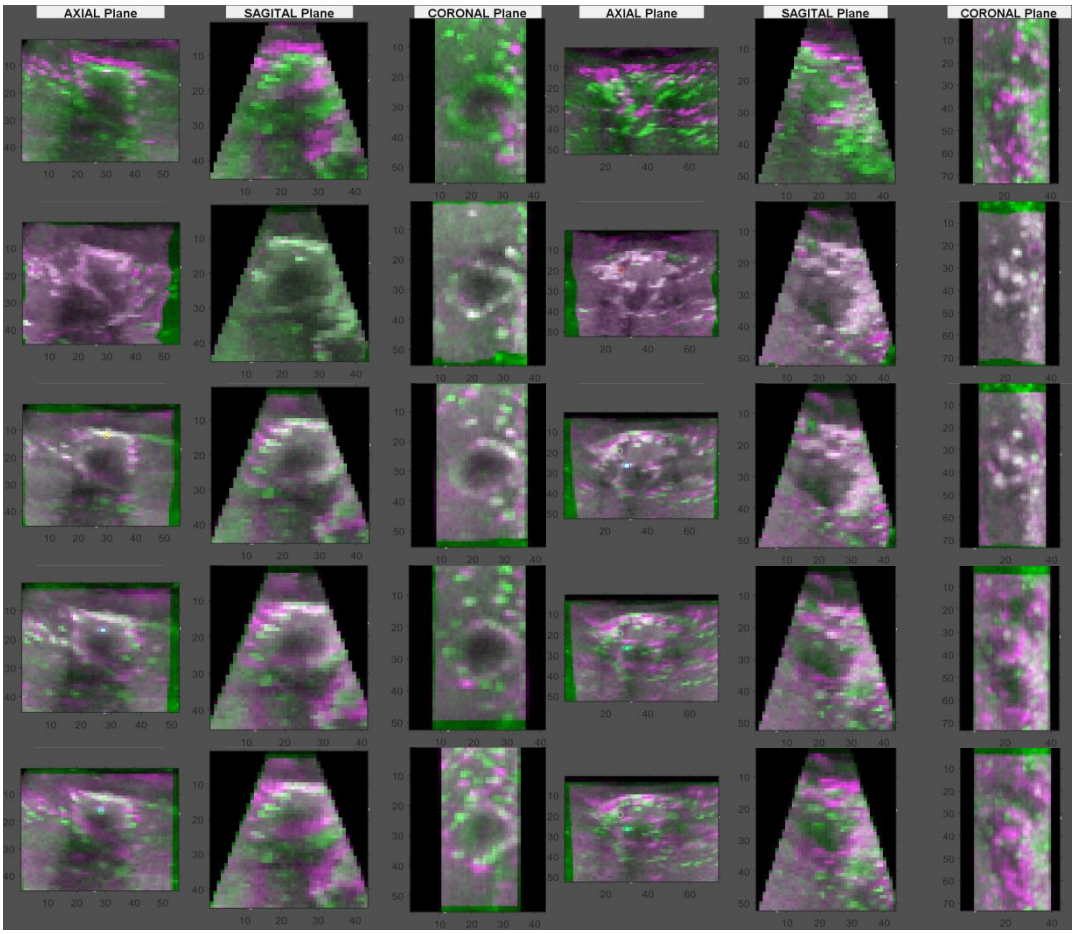

Figure 31 - Experiments varying the applied Accumulated Field Smoothing (AFS) in lesion 1(left) and lesion 2 (right). From up to bottom: Image with no registration; 0.5 AFS; 1.0 AFS; 1.5 AFS; 2.0 AFS.

A few experiments were carried regarding the influence of the previously described arguments. Mostly, better outcomes were achieved with 4 pyramid levels, with 200, 100, 50 and 25 iterations, respectively. The optimal accumulated field smoothing has the greater impact of all the arguments with values varying among samples, but globally better outcomes are achieved with ranges between 1 and 1.5. Some tests are depicted in *Figure 31*. Analyzing the images, one can easily see the effect of the smoothing factor, for example on the second images (from up to down) it is possible to see the effect of local deformations. For values higher than 2.0 (lowest images) the algorithm becomes more inaccurate and therefore these values are not ideal for the

desired application.

As previously explained, demons algorithm focus on local transformations in order to achieve the image alignment - voxels are pushed into or out of object boundaries to allow for image matching. This results in a calculated transformation for each pixel and is therefore difficult to quantify the target displacement based on the resultant image displacement field. In order to quantify the translation of the lesions an approach was implemented taking advantage of known fixed structures or points that may exist within the lesions. By selecting a point in the fixed image the displacement associated to its corresponding voxel and its immediate voxel neighbors, in all directions, is calculated. Next, the mean displacement of this group of voxels is calculated functioning as a surrogate for the lesion displacement in X, Y and Z.

4. Results

4.1. *Data Processing*

For the test images acquisition the US-Robot setup was used, as shown in *Figure 32*. At the same time, this was also a means to test the efficacy of the robot setup, using KUKA's positioning control in order to continuously acquire US image volumes while maintaining the probe in the defined position. This ensures that both the fixed and moving images are positioned in the same referential and therefore displacement estimation can be performed more accurately.

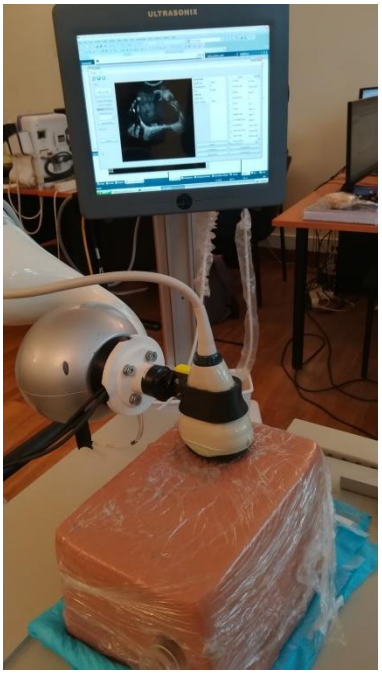

Figure 32 - 3D US Image acquisition of the liver phantom using the US-Robot setup.

As stated on the rationale of this work, the main tests and experiments that were executed aimed at testing the performance of non-rigid image registration algorithms for accurate measurements of liver tumor displacements. When tracking for tumor motion in IGRT techniques the most important deviations occur in the superior-inferior, anterior-posterior and medial-lateral directions, hierarchically. Deviations in these directions are therefore expressed by translational transformations. Nevertheless, these translations may be influenced by other type of transformations caused by tissue deformation such as compression or stress [19]. The formulated hypothesis is based on the concept that by allowing more degrees of freedom to the image registration algorithm the impact of tissue deformation could be minimized resulting in a more accurate translational displacement measurement.

For the evaluation of the image registration algorithms performance an error metric was used resorting to the estimated mean points (MP) of the implanted FM (fixed MP and moving MP in the fixed and moving images, respectively). This error was estimated by applying the achieved translational shift (from the moving image to the fixed) to the fixed MP. This point was then plotted in the moving image and the difference between it and the moving MP was calculated, resulting in the error associated to the algorithm under test. *Figure 33* is a schematic representation of the described process.

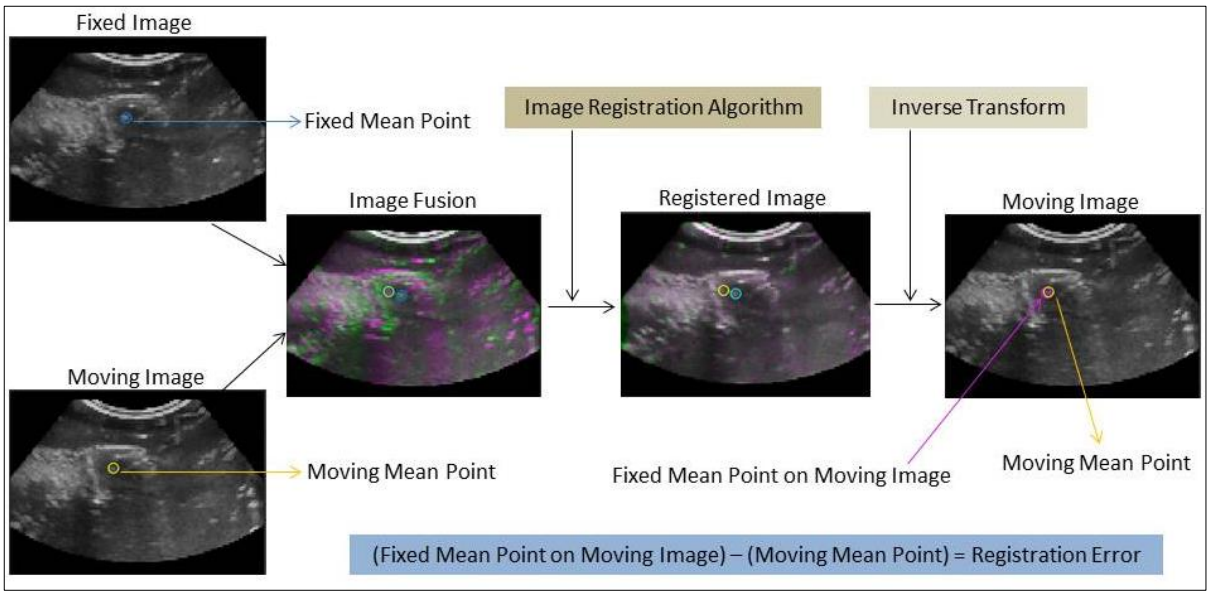

Figure 33 - Schematic representation of the image registration error calculation process.

Each algorithm was tested for each lesion and for all the displacement conditions. Two different scenarios were used to study the performance of the algorithms according to the available image information. More specifically two different FOV were used, one with the ROI adjusted to the lesion boundaries and the other using the entire image for the registration process.

Due to the clinical purpose of the BiPAP ventilator used to impose a physiological behaviour to the 4D liver phantom there is a limit to the pressure levels that is possible to pump, consequently this created a limitation on the the amount of movement that could be imposed to the tissue mimicking phantom. To overcome this issue and allow for the implementation of bigger displacements a in-exsufflator device was used (*Figure 34*). Thus being possible to test the system in more extreme conditions.

Figure 34 - In-exsufflator device

With the assitance of the previously mentioned device, four stages of pressure were used to create different moving images (25 cmH_2O, 35 cmH_2O, 45 cmH_2O and 55 cmH_2O), the increament in pressure level corresponds to an increase on the imposed displacement and deformations (*Figure 35*). The fixed images were acquired with 0 cmH_2O. Additionally an extreme deformation test was added in order to evaluate the performance and response of the implemented algorithm to higher levels of deformation.

The achieved outcomes will be presented and discussed on the following paragraphs.

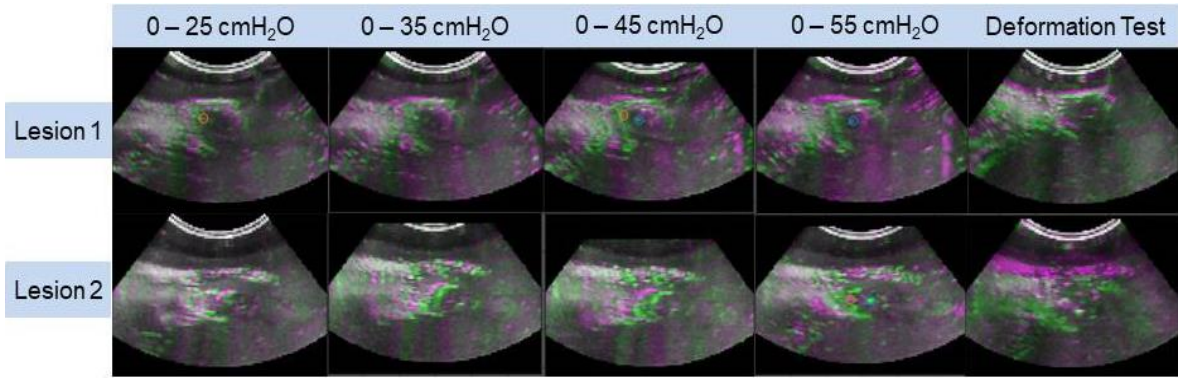

Figure 35 - Initial displacement illustration for the 2 lesions and pressure displacements. Fixed image displayed in green and moving in purple.

4.2. *Data Analysis*

4.2.1. Whole Volume Registration

Tables 3 shows the registration error for each algorithm in all displacement tests, for both lesions, taking the entire volume into account for the registration process. In *Table 4* the mean error for each algorithm is calculated as well as the respective standard deviation.

Table 3 - Registration error for each algorithm in all displacement tests, for both lesions, considering the entire volume.

Whole Image		0-25 (cmH_20)			0-35 (cmH_20)			0-45 (cmH_20)			0-55 (cmH_20)		
		SI (mm)	AP (mm)	ML (mm)	SI (mm)	AP (mm)	ML (mm)	SI (mm)	AP (mm)	ML (mm)	SI (mm)	AP (mm)	ML (mm)
Lesion 1	AIR	-2,61	-1,01	1,40	-4,14	-0,80	0,50	-7,48	-2,23	-0,45	-9,80	-2,73	-1,94
	DIR	0,13	-0,40	0,49	0,57	0,35	-0,28	0,02	-0,51	-0,93	0,71	-0,50	-0,53
	HIR	-0,68	-0,59	0,52	-0,73	0,14	-0,38	-1,69	-0,83	-1,09	-0,69	-0,73	-0,86
	MIR	-1,00	-0,68	-0,36	-0,88	0,20	-0,50	-0,17	-0,85	-1,00	0,45	-0,32	-0,50
Lesion 2	AIR	-2,69	-0,49	0,93	-3,35	-1,01	-1,99	-7,46	-1,50	-3,02	-10,19	-1,29	-1,01
	DIR	-0,59	-0,31	-0,89	1,06	-0,84	-1,10	0,85	-1,41	-0,96	1,08	-1,40	-0,57
	HIR	-0,74	-0,42	-0,68	0,40	-0,91	-1,31	-0,07	-1,30	-1,07	-1,18	-1,11	-0,42
	MIR	-0,53	0,03	0,50	0,03	0,06	-1,00	0,01	-0,41	-1,00	0,66	-0,18	-0,50

Table 4 – Mean error for each algorithm and respective standard deviation for the whole volume scenario

	Mean			Std Dev.		
	SI (mm)	AP (mm)	ML (mm)	SI (mm)	AP (mm)	ML (mm)
AIR	-5,97	-1,38	-0,70	3,15	0,75	1,57
DIR	0,48	-0,63	-0,60	0,58	0,59	0,52
HIR	-0,67	-0,72	-0,66	0,63	0,44	0,58
MIR	-0,18	-0,27	-0,55	0,59	0,37	0,50

By analyzing the values above it is possible to quickly realize the expressive errors from the AIR algorithm, especially in the SI direction with a mean error of -5,97 mm ± 3,15 mm. DIR performs generally well, displaying its highest error in the AP direction, on the 0-55 (cmH_2O) test which is the highest tested level of displacement. Globally, DIR demonstrates a steady and robust performance with mean errors well under 1 mm. Simultaneously, HIR also demonstrates good performance even though mean errors are slightly superior when compared to DIR algorithm.

4.2.2. Adjusted ROI Registration

Similarly to the previous section, *Table 5* shows the registration error for each algorithm in all displacement tests, for both lesions. In this case only an adjusted ROI is considered in the registration process. In *Table 6* the mean error for each algorithm is calculated as well as the respective standard deviation for the adjusted ROI scenario.

Table 5 - Registration error for each algorithm in all displacement tests, for both lesions, considering a ROI adjusted to lesion boundaries.

Adjusted ROI		0-25 (cmH_20)			0-35 (cmH_20)			0-45 (cmH_20)			0-55 (cmH_20)		
		SI (mm)	AP (mm)	ML (mm)	SI (mm)	AP (mm)	ML (mm)	SI (mm)	AP (mm)	ML (mm)	SI (mm)	AP (mm)	ML (mm)
Lesion 1	AIR	0,18	-0,33	-0,23	0,25	-0,36	-0,11	-0,38	-0,55	0,06	-1,02	-0,83	-0,62
	DIR	0,31	-0,21	-0,69	0,42	-0,36	-0,64	-0,28	-0,67	-0,52	0,23	-0,67	-0,05
	HIR	-0,04	-0,33	-0,66	0,04	-0,55	-0,68	-0,70	-1,05	-0,65	-1,20	-1,61	-0,33
	MIR	0,61	0,00	-0,50	0,01	0,10	0,00	-0,13	-0,54	-0,50	-0,52	-0,72	0,00
Lesion 2	AIR	-0,40	-0,58	0,65	-0,07	-0,54	-0,89	-0,14	-0,35	-1,74	-0,15	-0,60	-1,05
	DIR	-0,19	-0,56	-0,56	-0,02	-0,51	-0,36	-0,33	-0,26	-0,29	0,36	-1,21	-0,62
	HIR	-0,24	-0,54	-0,50	-0,15	-0,48	-0,43	-0,31	-0,32	-0,46	0,12	-2,12	-0,58
	MIR	-0,02	-1,04	0,50	-0,18	-0,70	-0,50	-0,63	-0,06	-1,00	-0,26	-0,18	-0,50

Table 6 – Mean error for each algorithm and respective standard deviation for the adjusted ROI scenario

	Mean			Std Dev.		
	SI (mm)	AP (mm)	ML (mm)	SI (mm)	AP (mm)	ML (mm)
AIR	-0,22	-0,52	-0,49	0,40	0,17	0,74
DIR	0,06	-0,56	-0,47	0,30	0,32	0,22
HIR	-0,31	-0,87	-0,53	0,44	0,67	0,13
MIR	-0,14	-0,39	-0,31	0,38	0,41	0,46

Opposite to what was found in the previous scenario, all registration algorithms achieve optimal performances when a ROI is defined encompassing the lesion boundaries. In this case, the AIR has similar results has the DIR method and punctually outperforms the last. Globally all the tested methods achieve mean errors inferior to 1 mm, in all directions.

4.2.3. Deformation Test

In *Table 7,* the registration errors achieved from the deformation test are detailed, for both scenarios, all registration methods and for lesion 1 and 2.

Table 7 - registration errors achieved from the deformation test for both scenarios, all registration methods and for lesion 1 and 2.

Deformation Test		Whole Image			Adjusted ROI		
		SI (mm)	AP (mm)	ML (mm)	SI (mm)	AP (mm)	ML (mm)
Lesion 1	AIR	0,71	-1,90	0,87	0,03	0,18	0,60
	DIR	2,66	0,05	0,09	0,69	0,83	-0,35
	HIR	2,06	0,56	-0,39	-0,19	-0,63	-0,10
	MIR	0,18	-0,59	0,00	0,26	-0,76	0,00
Lesion 2	AIR	0,60	-8,97	-2,02	-0,43	-0,03	-1,51
	DIR	0,75	-0,79	-0,67	-0,06	0,13	-0,02
	HIR	0,28	-1,98	-0,25	-0,30	0,29	-0,70
	MIR	-0,56	0,36	-0,50	-0,42	0,42	-0,50

The whole volume scenario shows the most controversial results with the DIR method standing out for achieving worse results than the other algorithms, for lesion 1, and AIR for lesion 2. In the adjusted ROI scenario all the algorithms perform exceptionally well. Nevertheless, DIR still under performs in lesion 1 when

compared to the other methods.

More controversial are perhaps the graphical results of this test (illustrated in *Figure 36*), where we can clearly notice that, in spite of achieving a larger errors than the other approaches, DIR and HIR registration perform more accurate registrations when it comes to image warping.

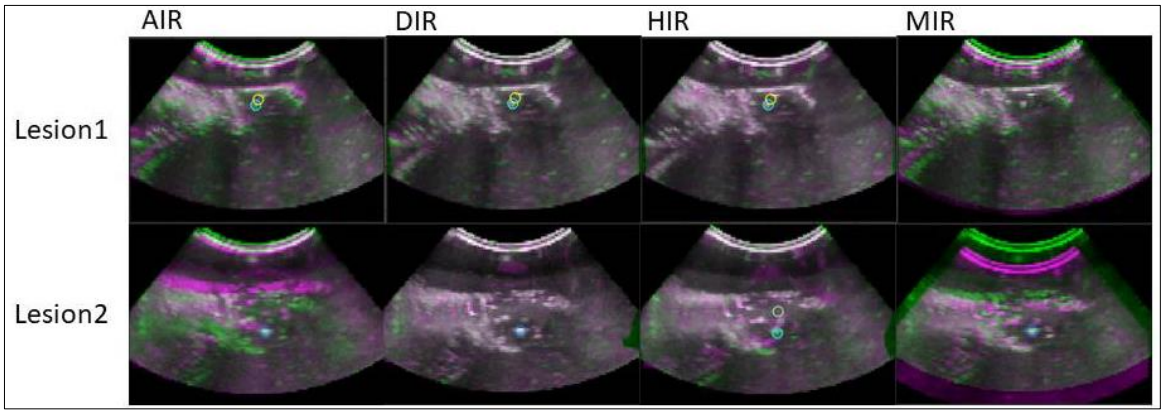

Figure 36 - Deformation registrations, for both lesions using the four implemented registration methods.

It is important to mention that this was meant to be an extreme deformation test, manually pressure was applied to achieve the desired deformation and so the applied force was not quantified.

4.3. ***Discussion***

The previously detailed data show that all implemented image registration algorithms perform well under certain conditions.

More specifically, when a ROI is defined encompassing the lesion boundaries all methods work exceptionally well, with mean errors under 1 mm, in all directions. In this scenario the affine algorithm outperforms the other automatic approaches (DIR and HIR) in some of the tests. On the other hand, when the whole volume is used the AIR method is incapable of achieving satisfactory results, while, the demons algorithm appears to achieve its best performance under these conditions. *Figure 37* exemplifies this relation between the implemented registrations for both scenarios.

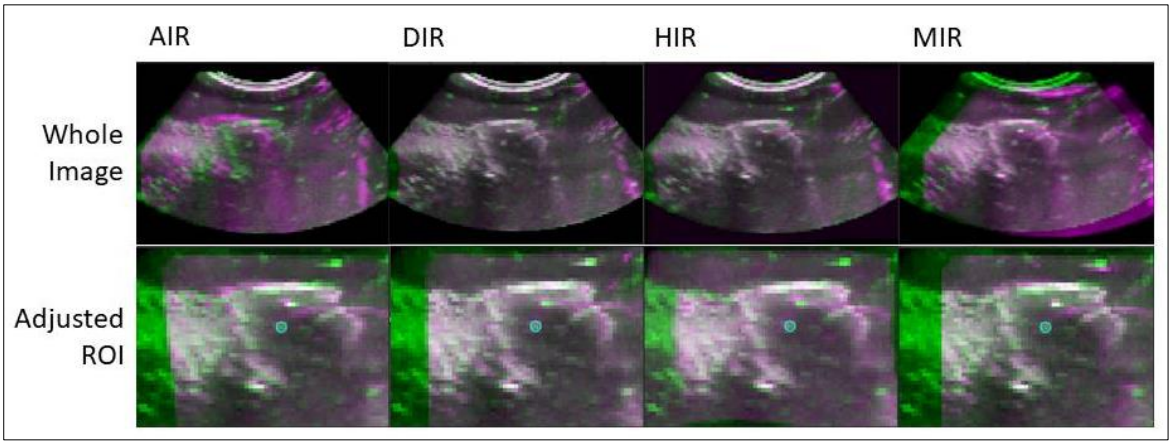

Figure 37 - Registration performance of the implemented methods, for both scenarios (0-55 cmH_2O test).

Given the formerly mentioned facts, and considering that affine consists in a global transformation, the poor outcomes of this algorithm in the whole image scenario are expected since the algorithm is not capable of matching all the detected intensities and still preserve image topology. Demons, however, is able of performing local transformations and does not necessarily preserves image topology. This could also be the reason for the controversial outcomes in the deformation test, proving that Demons registration is able of performing more accentuated local deformations, for example, to the lesion boundaries and act with less power in the center region of the lesion, resulting in a small global translation.

The implemented Hybrid algorithm, also demonstrates the ability to perform well in both scenarios and, although consisting on a two-step process with an affine transformation on the first step, results indicate that it is not negatively influenced by the same limitations as the AIR.

From the implemented automated image registration algorithms, DIR and HIR appear to perform better and be more consistent independently of the presented scenario, being less influenced by the amount of information in the FOV. This could be a determinant factor in a clinical application, since the aim is to be capable of tracking the displacement associated to a moving lesion and therefore a small ROI cannot be used.

All algorithms perform reasonably fast. Nevertheless, HIR involves the combination of both AIR and DIR and consequently has a higher computational load.

Manual Image Registration was also performed for the previously mentioned tests. This was meant to work as both a control for the automated methods and an assessment of consistency for manually performed image registration. Registered outcomes show that MIR is able to perform consistently well with similar or fewer mean errors than the automated approaches. Nonetheless it is important to mention that it is user dependent time consuming task and that the user could be influenced by the automated results during the registration process.

Finally, it is also important to note that ROI and point definition in the image registration application is a manual task and can, therefore, introduce some variability to the performed tests. Even so, the registered outcomes appear to be coherent and show little variability.

5. Conclusions

5.1. *Final considerations*

Upon the completion of this work we are able to conclude that using a robotic-US setup for adequate continuous 3D US image acquisition is feasible.

The KUKA robotic arm proves to be capable of holding the US probe continuously in the same position while contrary forces are imposed by the 4D US Phantom breathing-like motion.

The developed phantom also proves to be able to mimic physiological behavior expanding and contracting as inflated air pressure varies causing the 'liver-like' tumors to move and deform accordingly, and providing a good testing tool for preliminary tests and system calibration. Furthermore, it was shown during this experiment that breathing imposed tumor displacements are consistent with the expected physiological behavior, being more expressive in the SI direction.

As for the employment of non-rigid image registration algorithms for tumor tracking, it was shown that all the tested algorithms are able to perform with good level of accuracy when a ROI encompassing the lesion boundaries is defined. However, when the whole volume is used, AIR fails to adequately track the lesion. Both DIR and HIR indicate to have the largest potential to work under any scenario though, the implementation of a two-step algorithm (HIR) does not necessarily outperform the other methods and increases computational load without clear benefit. Demons method alone demonstrates to be the most adequate for the proposed application, presenting the possibility to overcome the use of FM as surrogates for IGRT techniques.

Further developments could be made to this US-robotic setup adding, for example, force control algorithms to the robotic arm in order to ensure patient safety or remote probe manipulation for fast small adjustments in the US image acquisition. More tests should be made to the performance of the DIR method in other scenarios, with different lesions or with higher displacements. Finally, this robotic assisted tool can only be considered adequate for clinically use after appropriate validation in Human subjects and, given the relevance of this application for IGRT techniques, further efforts should be made in this direction.

Bibliography

[1] Y. Seppenwoolde, W. Wunderink, S. R. W. Veen, P. Storchi, a M. Romero, and B. J. M. Heijmen, “Treatment precision of image-guided liver SBRT using implanted fiducial markers depends on marker-tumour distance.,” *Phys. Med. Biol.*, vol. 56, no. 17, pp. 5445–5468, 2011.

[2] L. Maier-Hein, C. J. Walsh, A. Seitel, N. C. Hanumara, J.-A. Shepard, a. M. Franz, F. Pianka, S. a. Müller, B. Schmied, A. H. Slocum, R. Gupta, and H.-P. Meinzer, “Human vs. robot operator error in a needle-based navigation system for percutaneous liver interventions,” *Proc. SPIE*, p. 72610Y–72610Y–12, 2009.

[3] S. R. Z. Abdel-Misih and M. Bloomston, “Liver Anatomy,” *Surg. Clin. North Am.*, vol. 90, no. 4, pp. 643–653, 2010.

[4] G. Oldrini, H. Taste-George, S. Renard-Oldrini, a. S. Baumann, V. Marchesi, P. Troufléau, D. Peiffert, a. Didot-Moisei, B. Boyer, B. Grignon, and P. Henrot, “Implantation of fiducial markers in the liver for stereotactic body radiation therapy: Feasibility and results,” *Diagn. Interv. Imaging*, pp. 1–4, 2014.

[5] D. Roberge and T. Cabrera, “Percutaneous Liver Fiducial Implants : Techniques , Materials and Complications,” no. Figure 1, 2010.

[6] W. Yang, B. a Fraass, R. Reznik, N. Nissen, S. Lo, L. H. Jamil, K. Gupta, H. Sandler, and R. Tuli, “Adequacy of inhale/exhale breathhold CT based ITV margins and image-guided registration for free-breathing pancreas and liver SBRT.,” *Radiat. Oncol.*, vol. 9, p. 11, 2014.

[7] C. Western, D. Hristov, and J. Schlosser, “Ultrasound Imaging in Radiation Therapy: From Interfractional to Intrafractional Guidance,” *Cureus*, vol. 7, no. 6, pp. 1–19, 2015.

[8] B. Presles, M. Fargier-Voiron, M. C. Biston, R. Lynch, a Munoz, H. Liebgott, P. Pommier, S. Rit, and D. Sarrut, “Automated registration of 3D transabdominal ultrasound images for patient repositioning before post-prostatectomy readiotherapy,” *Med. Phys.*, no. July 2015, 2014.

[9] S. Standring, H. Ellis, J. Healy, D. Johnson, and A. Williams, *Gray’s anatomy. 40th*. 2005.

[10] L. Sibulesky, “Normal liver anatomy,” *Clinical Liver Disease*, vol. 2, no. SUPPL. 1. pp. 2012–2014, 2013.

[11] D. V. Sahani, “Imaging the Liver,” *Oncologist*, vol. 9, no. 4, pp. 385–397, 2004.

[12] B. Ariff, C. R. Lloyd, S. Khan, M. Shariff, A. V Thillainayagam, D. S. Bansi, S. A. Khan, S. D. Taylor-robinson, A. K. P. Lim, B. Ariff, C. R. Lloyd, S. Khan, and A. K. P. Lim, “Imaging of liver cancer,” vol. 15, pp. 1289–1300, 2009.

[13] R. Lencioni, A. L. Baert, and K. Sartor, *Focal Liver Lesions*. .

[14] J. Bates, “Manual of diagnostic ultrasound,” *Ultrasound Med. Biol.*, vol. 22, no. 6, p. 767, 1996.

[15] T. Kron, “New developments in image guidance for radiotherapy,” *Cancer Forum*, vol. 36, no. 2, 2012.

[16] D. Fontanarosa, S. van der Meer, J. Bamber, E. Harris, T. O’Shea, and F. Verhaegen, “Review of ultrasound image guidance in external beam radiotherapy: I. Treatment planning and inter-fraction

motion management," *Phys. Med. Biol.*, vol. 60, no. 3, pp. R77–R114, 2015.

[17] L. a Dawson and C. Ménard, "Imaging in radiation oncology: a perspective.," *Oncologist*, vol. 15, no. 4, pp. 338–349, 2010.

[18] K. Cao, B. Bednarz, L. S. Smith, T. K. F. Foo, and K. a. Patwardhan, "Respiration induced fiducial motion tracking in ultrasound using an extended SFA approach," vol. 9419, p. 94190S, 2015.

[19] I. Buzurovic, T. K. Podder, K. Huang, and Y. Yu, "Tumor motion prediction and tracking in adaptive radiotherapy," *10th IEEE Int. Conf. Bioinforma. Bioeng. 2010, BIBE 2010*, pp. 273–278, 2010.

[20] A. Michalski, J. Atyeo, J. Cox, and M. Rinks, "Inter- and intra-fraction motion during radiation therapy to the whole breast in the supine position: A systematic review," *J. Med. Imaging Radiat. Oncol.*, vol. 56, no. 5, pp. 499–509, 2012.

[21] K. K. Brock and L. a Dawson, "Adaptive Management of Liver Cancer Radiotherapy," *Semin Radiat Oncol*, vol. 20, no. 2, pp. 107–115, 2010.

[22] T. Depuydt, D. Verellen, O. Haas, T. Gevaert, N. Linthout, M. Duchateau, K. Tournel, T. Reynders, K. Leysen, M. Hoogeman, G. Storme, and M. De Ridder, "Geometric accuracy of a novel gimbals based radiation therapy tumor tracking system," *Radiother. Oncol.*, vol. 98, no. 3, pp. 365–372, 2011.

[23] G. G. Zhang, H. M. Yu, C. W. Stevens, T. J. Dilling, S. E. Hoffe, and E. G. Moros, "Nuclear Medicine & Radiation Therapy Motion Management in Stereotactic Body Radiotherapy," 2012.

[24] E. S. Worm, M. Høyer, W. Fledelius, and P. R. Poulsen, "Three-dimensional, time-resolved, intrafraction motion monitoring throughout stereotactic liver radiation therapy on a conventional linear accelerator," *Int. J. Radiat. Oncol. Biol. Phys.*, vol. 86, no. 1, pp. 190–197, 2013.

[25] D. Habermehl, K. Henkner, S. Ecker, O. Jäkel, J. Debus, and S. E. Combs, "Evaluation of different fiducial markers for image-guided radiotherapy and particle therapy," *J. Radiat. Res.*, vol. 54, no. SUPPL.1, pp. 61–68, 2013.

[26] J.-E. Bibault, B. Prevost, E. Dansin, X. Mirabel, T. Lacornerie, and E. Lartigau, "Image-Guided Robotic Stereotactic Radiation Therapy with Fiducial-Free Tumor Tracking for Lung Cancer," *Radiat. Oncol.*, vol. 7, no. 1, p. 102, 2012.

[27] A. P. Shah, P. a. Kupelian, T. R. Willoughby, and S. L. Meeks, "Expanding the use of real-time electromagnetic tracking in radiation oncology.," *J. Appl. Clin. Med. Phys.*, vol. 12, no. 4, p. 3590, 2011.

[28] R. D. Foster, D. a Pistenmaa, and T. D. Solberg, "A comparison of radiographic techniques and electromagnetic transponders for localization of the prostate," *Radiat. Oncol.*, vol. 7, no. 1, p. 101, 2012.

[29] C. Gaisberger, P. Steininger, B. Mitterlechner, S. Huber, H. Weichenberger, F. Sedlmayer, and H. Deutschmann, "Three-dimensional surface scanning for accurate patient positioning and monitoring during breast cancer radiotherapy," *Strahlentherapie und Onkol.*, vol. 189, no. 10, pp. 887–893, 2013.

[30] M. Krengli, S. Gaiano, E. Mones, A. Ballarè, D. Beldì, C. Bolchini, and G. Loi, "Reproducibility of

patient setup by surface image registration system in conformal radiotherapy of prostate cancer.," *Radiat. Oncol.*, vol. 4, p. 9, 2009.

[31] R. Calow, G. Gademann, G. Krell, R. Mecke, B. Michaelis, N. Riefenstahl, and M. Walke, "Photogrammetric measurement of patients in radiotherapy," *ISPRS J. Photogramm. Remote Sens.*, vol. 56, no. 5–6, pp. 347–359, 2002.

[32] L. Deantonio, L. Masini, G. Loi, G. Gambaro, C. Bolchini, and M. Krengli, "Detection of setup uncertainties with 3D surface registration system for conformal radiotherapy of breast cancer," *Reports Pract. Oncol. Radiother.*, vol. 16, no. 3, pp. 77–81, 2011.

[33] Kasaova, "Quantitative Evaluation of the Benefit of Fiducial Image-Guidance for Prostate Cancer Intensity Modulated Radiation Therapy using Daily Dose Volume Histogram Analysis," *Technol. Cancer Res. Treat.*, vol. 13, no. 1, 2013.

[34] C.-H. Liu, C.-Y. Yu, T.-P. Lin, H.-L. Chao, H.-C. Chen, and C.-C. Cheng, "Sonographic-guided percutaneous fiducial marker implantation of hepatic malignancies for Cyberknife radiation therapy: Evaluation of safety and technical efficacy," *J. Med. Sci.*, vol. 35, no. 3, p. 92, 2015.

[35] M. Lachaine and T. Falco, "Intrafractional prostate motion management with the Clarity Autoscan system," *Med. Phys. Int.*, vol. 1, no. 1, pp. 72–80, 2013.

[36] F. L. B. Cury, G. Shenouda, L. Souhami, M. Duclos, S. L. Faria, M. David, F. Verhaegen, R. Corns, and T. Falco, "Ultrasound-based image guided radiotherapy for prostate cancer-comparison of cross-modality and intramodality methods for daily localization during external beam radiotherapy," *Int. J. Radiat. Oncol. Biol. Phys.*, vol. 66, no. 5, pp. 1562–1567, 2006.

[37] R. Ramer, "B-mode Acquisition and Targeting (BAT) Ultrasound for Image-Guided Radiotherapy," 2005.

[38] W. Wein, B. Roper, and N. Navab, "Integrating Diagnostic <emphasis>B</emphasis>-Mode Ultrasonography Into CT-Based Radiation Treatment Planning," *IEEE Trans. Med. Imaging*, vol. 26, no. 6, pp. 866–879, 2007.

[39] D. Robinson, D. Liu, S. Steciw, C. Field, H. Daly, E. P. Saibishkumar, G. Fallone, M. Parliament, and J. Amanie, "An evaluation of the Clarity 3D ultrasound system for prostate localization.," *J. Appl. Clin. Med. Phys.*, vol. 13, no. 4, p. 3753, 2012.

[40] J. Boda-Heggemann, F. M. Köhler, B. Küpper, D. Wolff, H. Wertz, S. Mai, J. Hesser, F. Lohr, and F. Wenz, "Accuracy of Ultrasound-Based (BAT) Prostate-Repositioning: A Three-Dimensional On-Line Fiducial-Based Assessment With Cone-Beam Computed Tomography," *Int. J. Radiat. Oncol. Biol. Phys.*, vol. 70, no. 4, pp. 1247–1255, 2008.

[41] K. Peignaux, G. Truc, I. Barillot, A. Ammor, S. Naudy, G. Créhange, and P. Maingon, "Clinical assessment of the use of the Sonarray system for daily prostate localization," *Radiother. Oncol.*, vol. 81, no. 2, pp. 176–178, 2006.

[42] E. Bloemen-Van Gurp, S. Van Der Meer, J. Hendry, J. Buijsen, P. Visser, D. Fontanarosa, M. Lachaine, G. Lammering, and F. Verhaegen, "Active breathing control in combination with ultrasound

imaging: A feasibility study of image guidance in stereotactic body radiation therapy of liver lesions," *Int. J. Radiat. Oncol. Biol. Phys.*, vol. 85, no. 4, pp. 1096–1102, 2013.

[43] P. Wong, T. Muanza, E. Reynard, K. Robert, J. Barker, and K. Sultanem, "Use of three-dimensional ultrasound in the detection of breast tumor bed displacement during radiotherapy," *Int. J. Radiat. Oncol. Biol. Phys.*, vol. 79, no. 1, pp. 39–45, 2011.

[44] J. a Molloy, G. Chan, A. Markovic, S. McNeeley, D. Pfeiffer, B. Salter, and W. a Tome, "Quality assurance of U.S.-guided external beam radiotherapy for prostate cancer: report of AAPM Task Group 154.," *Med. Phys.*, vol. 38, no. 2, pp. 857–871, 2011.

[45] M. Fargier-Voiron, B. Presles, P. Pommier, S. Rit, A. Munoz, H. Liebgott, D. Sarrut, and M. C. Biston, "Impact of probe pressure variability on prostate localization for ultrasound-based image-guided radiotherapy," *Radiother. Oncol.*, vol. 111, no. 1, pp. 132–137, 2014.

[46] J. Schlosser, K. Salisbury, and D. Hristov, "Telerobotic system concept for real-time soft-tissue imaging during radiotherapy beam delivery.," *Med. Phys.*, vol. 37, no. 12, pp. 6357–6367, 2010.

[47] H. T. Sen, M. a L. Bell, I. Iordachita, J. Wong, and P. Kazanzides, "A cooperatively controlled robot for ultrasound monitoring of radiation therapy," *IEEE Int. Conf. Intell. Robot. Syst.*, pp. 3071–3076, 2013.

[48] M. a. L. Bell, H. T. Sen, I. Iordachita, P. Kazanzides, and J. Wong, "*In vivo* reproducibility of robotic probe placement for a novel ultrasound-guided radiation therapy system," *J. Med. Imaging*, vol. 1, no. 2, p. 25001, 2014.

[49] M. Ingenieurwissenschaft and I. Kuhlemann, "Force and Image Adaptive Strategies for Robotised Placement of 4D Ultrasound Probes."

[50] J. Schlosser, K. Salisbury, and D. Hristov, "Online image-based monitoring of soft-tissue displacements for radiation therapy of the prostate," *Int. J. Radiat. Oncol. Biol. Phys.*, vol. 83, no. 5, pp. 1633–1640, 2012.

[51] T. P. O'Shea, L. J. Garcia, K. E. Rosser, E. J. Harris, P. M. Evans, and J. C. Bamber, "4D ultrasound speckle tracking of intra-fraction prostate motion: a phantom-based comparison with x-ray fiducial tracking using CyberKnife.," *Phys. Med. Biol.*, vol. 59, no. 7, pp. 1701–20, 2014.

[52] Y. Kubota, A. Matsumura, M. Fukahori, S. Minohara, S. Yasuda, and H. Nagahashi, "A new method for tracking organ motion on diagnostic ultrasound images," *Med. Phys.*, vol. 41, no. 9, p. 92901, 2014.

[53] M. a L. Bell, B. C. Byram, E. J. Harris, P. M. Evans, and J. C. Bamber, "In vivo liver tracking with a high volume rate 4D ultrasound scanner and a 2D matrix array probe," *Phys. Med. Biol.*, vol. 57, no. 5, pp. 1359–1374, 2012.

[54] G. Stetten and R. Tamburo, "Real-time three-dimensional ultrasound methods for shape analysis and visualization.," *Methods*, vol. 25, no. 2, pp. 221–230, 2001.

[55] E. J. Harris, N. R. Miller, J. C. Bamber, J. R. N. Symonds-Tayler, and P. M. Evans, "Speckle tracking in a phantom and feature-based tracking in liver in the presence of respiratory motion using 4D ultrasound.," *Phys. Med. Biol.*, vol. 55, no. 12, pp. 3363–3380, 2010.

[56] R. Bruder, F. Ernst, a Schlaefer, and a Schweikard, “Real-Time PV Tracking in 3D Ultrasound of the Beating Heart,” *Rob.Uni-Luebeck.De*, pp. 1–2, 2012.

[57] V. De Luca, T. Benz, S. Kondo, L. König, D. Lübke, S. Rothlübbers, O. Somphone, S. Allaire, M. a Lediju Bell, D. Y. F. Chung, a Cifor, C. Grozea, M. Günther, J. Jenne, T. Kipshagen, M. Kowarschik, N. Navab, J. Rühaak, J. Schwaab, and C. Tanner, “The 2014 liver ultrasound tracking benchmark,” *Phys. Med. Biol.*, vol. 60, no. 14, pp. 5571–5599, 2015.

[58] A. Myronenko, “Non-rigid Image Registration: Regularization, Algorithms and Applications,” *Regul. Algorithms Appl. a Diss.*, no. June, p. 316, 2010.

[59] M. Holden, “Nonrigid Body Registration OF PA VS WM,” *IEEE Trans. Med. Imaging*, vol. 27, no. 1, pp. 111–128, 2008.

[60] L. Tang and G. Amarneh, “Medical image registration: a review,” in *Medical Imaging: Technology and Applications*, T. Francombe and K. Iniewski, Eds. 2014, pp. 619–651.

[61] W. R. Crum, T. Hartkens, and D. L. G. Hill, “Non-rigid image registration: theory and practice,” *Br. J. Radiol.*, vol. 77, no. suppl_2, pp. S140–S153, 2004.

[62] F. P. M. Oliveira and J. M. R. S. Tavares, “Medical image registration: a review,” *Computer Methods in Biomechanics and Biomedical Engineering*, vol. 17, no. 2. Taylor & Francis, pp. 73–93, 2014.

[63] S. M. G, “Classification of Image Registration Techniques and Algorithms in Digital Image Processing – A Research Survey,” *Ijctt*, vol. 15, no. 2, pp. 78–82, 2014.

[64] J. M. Fitzpatrick, D. L. G. Hill, and C. R. Maurer, “Image Registration,” *Handb. Med. Imaging, Vol. Med. Image Process. Anal.*, pp. 447–514, 2000.

[65] I. M. J. van der Bom, S. Klein, M. Staring, R. Homan, L. W. Bartels, and J. P. W. Pluim, “Evaluation of optimization methods for intensity-based 2D-3D registration in x-ray guided interventions,” *Proc. SPIE*, vol. 7962, no. 1, pp. 796223-796223–15, 2011.

[66] L. Eikvil, P. O. Husøy, and A. Ciarlo, “Adaptive Image Registration,” *Proc. ESA-EUSC 2005 Image Inf. Min. - Theory Appl. to Earth Obs.*, no. 1, 2005.

[67] T. Vercauteren, X. Pennec, A. Perchant, and N. Ayache, “Diffeomorphic demons: efficient non-parametric image registration.,” *Neuroimage*, vol. 45, no. 1 Suppl, pp. S61–S72, 2009.

[68] R. Bischoff, J. Kurth, G. Schreiber, R. Koeppe, A. Albu-Schäffer, D. Beyer, O. Eiberger, S. Haddadin, A. Stemmer, G. Grunwald, and K. R. Gmbh, “The KUKA-DLR Lightweight Robot arm – a new reference platform for robotics research and manufacturing Summary / Abstract Stages of research and product de- velopment,” *Jt. 41th Internatiional Symp. Robot. 6th Ger. Conf. Robot.*, pp. 741–748, 2010.

[69] S. Tauscher, J. Tokuda, G. Schreiber, T. Neff, N. Hata, and T. Ortmaier, “OpenIGTLink interface for state control and visualisation of a robot for image-guided therapy systems,” *Int. J. Comput. Assist. Radiol. Surg.*, vol. 10, no. 3, pp. 285–292, 2015.

[70] H. Monnich, H. Worn, and D. Stein, “OP sense A robotic research platform for telemanipulated and

automatic computer assisted surgery," *Int. Work. Adv. Motion Control. AMC*, 2012.

[71] L. Maier-Hein, a Ftanz, H. P. Meinzer, and I. Wolf, "Comparative assessment of optical tracking systems for soft tissue navigation with fiducial needles - art. no. 69181Z," *Med. Imaging 2008 Vis. Image-Guided Proced. Model. Pts 1 2*, vol. 6918, no. 69181, pp. Z9181–Z9181, 2008.

[72] W. Birkfellner, J. Hummel, and E. Wilson, "Chapter 2 Tracking Devices," *Business*, pp. 23–45, 2008.

[73] J. B. West and C. R. Maurer, "Designing optically tracked instruments for image-guided surgery," *IEEE Trans. Med. Imaging*, vol. 23, no. 5, pp. 533–545, 2004.

[74] L. E. Bø, E. F. Hofstad, F. Lindseth, and T. A. N. Hernes, "Versatile robotic probe calibration for position tracking in ultrasound imaging," *Phys. Med. Biol.*, vol. 60, no. 9, pp. 3499–3513, 2015.

[75] K. Hamad, M. Kaseem, H. W. Yang, F. Deri, and Y. G. Ko, "Properties and medical applications of polylactic acid: A review," *Express Polym. Lett.*, vol. 9, no. 5, pp. 435–455, 2015.

[76] X. Pennec, P. Cachier, and N. Ayache, "Understanding the 'Demon's Algorithm': 3D non-rigid registration by gradient descent," *Int. Conf. Med. Image Comput. Comput. Interv.*, vol. 1679, pp. 597–605, 1999.

[77] B. B. Avants, C. L. Epstein, M. Grossman, and J. C. Gee, "Symmetric diffeomorphic image registration with cross-correlation: Evaluating automated labeling of elderly and neurodegenerative brain," *Med. Image Anal.*, vol. 12, no. 1, pp. 26–41, 2008.